Mechanics of Materials 175 (2022) 104500

Contents lists available at ScienceDirect

Mechanics of Materials

journal homepage: www.elsevier.com/locate/mechmat

# New double surface constitutive model of intermittent plastic flow applied to near 0 K adiabatic shear bands

Rafał Schmidt *, Błażej Skoczeń, Jan Bielski, Elwira Schmidt

*Faculty of Mechanical Engineering, Cracow University of Technology, 31-864, Cracow, Poland*

ARTICLE INFO

*Keywords:*
Plasticity
Shear bands
Intermittent plastic flow
Phase transformation
Cryogenic temperatures

ABSTRACT

One of the most interesting phenomena that occur in ductile materials strained in the proximity of absolute zero are the adiabatic shear bands. In the stainless steels, massively used to construct superconducting magnets, their occurrence can be detected by various techniques, including magnetometric methods (feritscope). Formation of adiabatic shear bands is strictly correlated to the occurrence of the intermittent plastic flow (IPF), characteristic of stainless steels strained in liquid or superfluid helium. Evidence for the occurrence of the phase transformation during nucleation and formation of the shear bands in the proximity of absolute zero is for the first time given. The rate of shear bands propagation along the sample as well as the amount of secondary phase is measured. In order to describe the intermittent plastic flow, novel double surface model has been developed. It includes type Huber-Mises-Hencky yield surface, and new recovery surface reflecting the lower bound for the stress oscillations. The yield surface can move and expand due to nonlinear mixed (kinematic and isotropic) hardening, resulting from the phase transformation, whereas, the recovery surface remains constant. The serrations occur between the yield surface and the recovery surface, with the yield surface coming back to its initial position after each serration. Each serration corresponds to formation of single shear band there, where the easy slip planes are available, and the mechanism of anchoring the shear bands by the secondary phase is explained. New double surface model has been correlated to the experimental data and applied to explain stress oscillations during the regular stage of the intermittent plastic flow, when the shear bands gradually cover the gauge length of the sample.

## 1. Introduction

Selection of the materials applied for construction of the cryogenic installations, including the superconducting particle accelerators, comprises large variety of stainless steels. Such grades like 304, 304L, 316, 316L or 316 LN are among the most popular because of their excellent physical and mechanical properties as well as moderate cost (Bayerlein et al., 1992; Kim et al., 2014). These materials show, however, metastable behaviour consisting in the plastic strain induced phase transformation from the face centred cubic (fcc) to the body centred cubic (bcc) lattice (Cherkaoui et al., 1998; Bracke et al., 2007; Garion et al., 2006; Das and Tarafder, 2009). The microstructure of the stainless steels of series 300 is dominated at room temperature by the classical face centred cubic austenite ($\gamma$ phase). The $\gamma$ phase usually transforms to the hexagonal $\varepsilon$ phase, and further to $\alpha'$ martensite, forming the bcc inclusions embedded in the surrounding austenitic matrix. During the plastic strain induced fcc-bcc phase transformation, the martensite fraction occupies larger volume than the pre-existing austenite, which leads to the additional strain component in the form of transformation induced strain. The volume fraction of secondary phase depends on the chemical composition, the temperature, the stress state, the plastic strain intensity and the exposure to magnetic field. It is well known that the solutes like Ni, Mn and N considerably stabilize $\gamma$ phase. In view of the possible applications, it is worth pointing out that the martensitic transformation may substantially affect formability of the austenitic stainless steel.

The phase transformation accompanies various types of plastic flow, including the smooth plastic flow (SPF) and the intermittent plastic flow (IPF) (Skoczeń et al., 2010; Skoczeń et al., 2014). The latter occurs at the temperatures below a threshold characteristic of given material (Zinov'ev et al., 1972; Estrin and Kubin, 1980; Estrin and Tangri, 1981; Kubin et al., 1982; Komnik et al., 1985; Burns, 1994; Han et al., 2018). Until now there was no clear evidence for simultaneous occurrence the IPF and the fcc-bcc phase transformation, apart from some indications

* Corresponding author.
*E-mail address:* rafal.schmidt@pk.edu.pl (R. Schmidt).

https://doi.org/10.1016/j.mechmat.2022.104500
Received 14 October 2021; Received in revised form 8 October 2022; Accepted 11 October 2022
Available online 15 October 2022

related to strain localization during the IPF in the form of the shear bands (Vinogradov et al., 2010; Wang et al., 2020). Also, a hypothesis has been forged that the phase transformation hindered apparent "motion" of the shear bands, however, it has not been experimentally confirmed. Formation of $\alpha'$ martensite in the course of the SPF was not questioned, whereas the evidence for the fcc-bcc phase transformation during the IPF was lacking (cf. Obst and Nyilas, 1991, 1998). In the present paper the experimental evidence for simultaneous occurrence of both phenomena is shown in the context of the strain localization during the IPF in the form of shear bands.

The problem of the shear bands formation, including the evolution of the secondary phase in the austenitic stainless steels subjected to thermo-mechanical loads, was studied – among others – by Diani and Parks (1998), in the context of the deformation mechanisms in the grains. Low stacking fault energy (LSFE) austenitic stainless steels were analysed. The shear bands formation was described in terms of an irreversible process, that does not induce significant volume change. In the constitutive model the classical theory of plasticity was used, with the mechanism of inelastic deformation dominated by the crystallographic slip. The nucleation of α′-martensite took place at the shear bands intersection. At extremely low temperatures two shear band formation mechanisms were essentially identified: twining and formation of ε-martensite. During the deformation, locking of the shear bands by the α′-martensite inclusions was observed. A study of coupling between the temperature fluctuations and the strain localization during the discontinuous plastic flow at cryogenic temperatures was developed by Tabin et al. (2016).

Constitutive modelling of the IPF (Vorob'ev, 2006, 2008; Brechtl et al., 2019) is crucial in view of more advanced applications of the stainless steels at extremely low temperatures. Following a broad review by Pustovalov (2008), an interesting study of the serrated yielding of austenitic steel and aluminium alloy at 4 K was published by Vorob'ev and Anpilogova (2013). The authors presented the influence of eight factors (including material and loading system characteristics) on the discontinuous deformation of metals. Another paper by Vorob'ev and Anpilogova (2015) dealt with the kinetics of the discontinuous yielding in an austenitic steel and an aluminium alloy at the temperature of 4 K. In particular, the energy balance and the mechanism of low-temperature discontinuous yielding in metals were explained. Quite recently, an interesting paper on the deformation of austenitic stainless steels at cryogenic temperatures was published by Han et al. (2018). The austenitic stainless steel (316LN), applied in the form of jacket material for low-temperature superconductors of fusion reactors, was analysed. Serrated yielding related to the specific motion of dislocations and the phase transformation was analysed. Another interesting study, highlighting the mechanical and the physical features of the serrated yielding in the high entropy alloys at cryogenic temperatures, was carried out by Tirunilai et al. (2020). The authors discuss CoCrFeMnNi alloy that exhibits serrated yielding, accompanied by the large drops of stress of the order of 100 MPa. An interesting feature of this alloy consists in the fact, that it shows the IPF at significantly higher temperatures (around 35 K) than previously reported. Moreover, it has been shown that the temperature and the dislocation density control serrated yielding, and there is an increase of the cross-slip difficulty with decreasing temperature. Finally, an effort to develop complex model of the intermittent plastic flow in the context of strain localization within the shear bands was presented by Tabin et al. (2016).

In the present paper, the experimental evidence for the phase transformation during each serration (single stress-strain oscillation) is shown, and a new constitutive model of the IPF is developed. Double surface (yield surface and recovery surface) constitutive model describes the regular part of the stress-strain oscillations during the IPF. The model includes the classical Huber-Mises-Hencky yield surface and new recovery surface, reflecting the lower bound of the stress oscillations (cf. Mróz, 1967). The yield surface can move and expand due to the nonlinear mixed hardening, resulting from the phase transformation, whereas, the recovery surface remains constant. In particular, the serrations occur between the yield surface and the recovery surface, with the yield surface coming back to its initial position after each serration. Also, the opinion that the intermittent plastic flow and the plastic strain induced phase transformation cannot coexist is in the present paper formally disproved. It is shown that during the intermittent plastic flow the favourable conditions for the fcc-bcc phase transformation occur, and a localized transformation may affect the conditions of the plastic flow. The amount of the phase transformation per serration, and the propagation velocity of the phase transformation front consisting in formation of the subsequent shear bands, are measured.

## 2. Strain induced phenomena at extremely low temperatures

Among various phenomena occurring in the materials at extremely low temperatures, two phenomena are of particular importance for maintaining the integrity of the continuum: the intermittent plastic flow and the plastic strain induced fcc-bcc phase transformation. In both cases, it is crucial to understand the mechanism behind the phenomenon and to correctly describe its kinetics.

### 2.1. Intermittent plastic flow (IPF)

Intermittent plastic flow represents the so-called oscillatory mode of plastic deformation, strictly related to the evolution of microstructure of the material in the course of yielding at extremely low temperatures. Both the low and the high stacking fault energy materials show this type of behaviour as long as the deformation process is kinematically controlled. An interesting feature of the IPF consists in the fact, that each serration is composed of several stages: elastic loading, smooth plastic flow, drop of stress at constant total strain and relaxation. The latter is not always present and depends on the amount of heat stored in the material in the course of single serration. In the previous paper (Tabin et al., 2016), it has been shown that the intermittent plastic flow is related to the formation of the shear bands. In particular, temperature measurements confirmed this fact, and the position of shear band was deduced from the temperature distribution. The main mechanism of the IPF was attributed to production of the lattice barriers, forming obstacles to the motion of dislocations. Such a mechanism is backed by the previous works, as well as more recent observations (Tabin et al., 2021). One of the most interesting features of the IPF is the fact, that it occurs below a threshold temperature, specific of given material: $T_1$ for the low stacking fault energy, and $T_0$ for the high stacking fault energy materials. It looks like each of these thresholds represents a transition from the domination of screw to the domination of the edge dislocations, which is rather difficult to confirm experimentally. Type of dislocations may depend on the temperature, especially at extremely low temperatures where a significant lack of the thermal energy is observed. Poor excitation of the lattice may significantly affect the generation and the motion of dislocations. As the edge dislocations move at very low temperatures at a lower stress than the screw dislocations, it is assumed that the edge dislocations dominate in the proximity of absolute zero. Generally, the threshold temperatures ($T_0$ and $T_1$) depend on the chemical composition of the material and - at least for the stainless steels - do not exceed some 35 K.

The initiation plastic strain to trigger the IPF (Fig. 1) is function of temperature, and for the liquid (4.2 K) or the superfluid (below 2.17 K) helium it practically reaches zero. Thus, in liquid helium the IPF occurs as soon as the plastic straining begins. For what concerns the strain rates, the intermittent plastic flow occurs for a wide range of the strain rates, starting from lower and ending up with upper critical level. The lower level is practically negligible, whereas, the upper level is a function of the chemical composition of the material, and as soon as it is reached nearly adiabatic heat accumulation leads to the fast increase of temperature beyond the threshold and – consequently – transition to the smooth plastic flow.

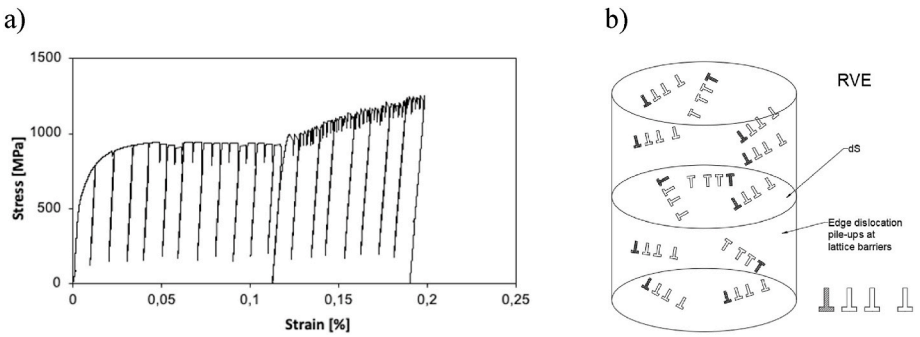


**Fig. 1.** Intermittent Plastic Flow in liquid helium: (a) behaviour of grade 316L stainless steel at 4.2 K in terms of the stress-strain serrations (short drops of stress), long drops indicate the unloading that apparently does not affect the serrations, (b) Representative Volume Element (RVE) containing representation of the edge dislocation pile-ups at the lattice barriers, with black symbols indicating the barriers and white symbols representing the dislocation pile-ups.

The interest in explaining the intermittent plastic flow can be traced back to the work by Seeger (1957), who indicated that the pile-ups of dislocations on the internal lattice barriers contribute to the stress concentrations of the order of the theoretical shear strength. However, two schools were essentially forming around the explanation of this phenomenon: the school of the adiabatic heating promoted by Basinski (1957) (cf. Shibata, 1988), and the school of the lattice barriers hindering the motion of dislocations, formulated by Obst and Nyilas (1991), 1998. Basinski developed the adiabatic heating hypothesis, stating that any sufficiently fast dissipative process at very low temperatures leads to such increase of the temperature, that drastic decrease of the flow stress is observed. This hypothesis has been contradicted by precise measurements of the force (stress), the elongation (strain) and the temperature, performed directly on the sample. It turns out, that the drop of stress precedes the temperature increase, which excludes the temperature being the trigger of the drop of stress. Another explanation was formulated by Obst and Nyilas (1991, 1998) who stated that the load drops are possibly due to a catastrophic process related to the spontaneous generation of the dislocations as soon as the lattice barriers are broken. Gröger and Zehetbauer (1993) presented the experimental results related to the intermittent plastic flow at low temperatures in the age-hardenable fcc alloy Cu·Be 2. The authors compared two approaches: the thermomechanical models (TMI) of Kubin and Estrin, and the model of Obst et al. making the mechanical processes responsible for the onset of the IPF. Yet another explanation of the intermittent plastic flow was offered by Zaiser and Hähner (1997), who attributed serrated yielding occurring at very low temperatures to the strain rate softening instabilities. Moreover, the authors indicated similar nature of the low temperature IPF and the room temperature Portevin–Le Chatelier (PLC) phenomenon. The explanation based on the strain rate sensitivity made direct reference to the behaviour of the strain ageing materials. A universal model of the intermittent plastic flow, including the above phenomena as well as the relevant thermodynamic background, was developed by Skoczeń et al., 2010.

### 2.2. Plastic strain induced fcc-bcc phase transformation

Generally, the fcc-bcc phase transformation may have spontaneous, stress assisted or strain induced character. A crucial role is played by the temperature $M_s^\sigma$ below which the stress assisted phase transformation takes place. In this range yielding is initiated by formation of the secondary phase (martensite). On the other hand, above $M_s^\sigma$, yielding is initiated in the parent phase by the classical slip mechanism (motion of the dislocations in the lattice). As the temperature of liquid helium (4.2 K) is – for typical stainless steels – lower than $M_s^\sigma$, yielding is usually initiated by the formation of martensite (transformation induced plasticity, TRIP), and later on by the classical slip. Since the amount of the martensite created below the apparent yield stress is small, the plastic strain induced fcc-bcc phase transformation will be further addressed.

The phenomenon of the phase transformation is first of all described by the transformation kinetics, that reflects the rate of transformation as a function of measurable variable – the plastic strain. The kinetics is usually illustrated by the phase transformation curve (Fig. 2), expressed in terms of the volume fraction of secondary phase ($\xi$) versus the plastic strain ($\varepsilon_p$). Originally, the kinetics of the plastic strain induced fcc-bcc phase transformation at very low temperatures was derived by Olson and Cohen (1972), 1975:

$$\xi = 1 - e^{-\beta\left(1-e^{-\alpha\varepsilon^p}\right)^n} \quad ; \quad \beta = \frac{v_\alpha k p_\alpha}{v^n} \tag{1}$$

Here, α is a parameter representing the rate of the shear band formation, $p_\alpha$ denotes the probability that a shear band intersection will generate martensitic embryo, whereas $v_\alpha$ stands for the constant volume of the martensitic site. The Olson-Cohen kinetics (1975) contains essentially three parameters: two of them are temperature dependent (α, β), and n is a fixed exponent.

The phase transformation at extremely low temperatures is much steeper in terms of $\xi_{,\varepsilon^p}$ than at room temperature, and can be subdivided into three stages (Fig. 2):

I. low transformation rate (below the threshold $\varepsilon_\xi^p$), $\xi_{,\varepsilon^p} \approx 0$,
II. high transformation rate (with constant slope), $\xi_{,\varepsilon^p} = A$,
III. asymptotically vanishing transformation (above the threshold $\varepsilon_L^p$), $\xi_{,\varepsilon^p} \approx 0$.

For the isothermal processes and small variations of stress, the linearized phase transformation kinetics reads (Garion et al., 2006; Sitko et al., 2010; Ortwein et al., 2014):

$$\xi_{,t} = A(T,\sigma)\varepsilon_{,t}^p \quad ; \quad \varepsilon_\xi^p \le \varepsilon^p \le \varepsilon_L^p \tag{2}$$

where $A(T,\sigma)$ stands for the constant slope during stage II, and $x_{,t} = \frac{dx}{dt}$ denotes the time derivative. Both the threshold strain $\varepsilon_\xi^p$ and the parameter $A$ depend on temperature and the chemical composition of the alloy. By integrating Eq. (2) one obtains:

$$\xi = \xi_0 + \Delta\xi = \xi_0 + \int_{\varepsilon_\xi^p}^{\varepsilon_L^p} A d\varepsilon^p \tag{3}$$

## 3. Fcc-bcc phase transformation induced by intermittent plastic flow

Until now, the opinion supported by several authors excluded the possibility of simultaneous occurrence of the intermittent plastic flow (serrated yielding) and the plastic strain induced fcc-bcc phase transformation. In particular, for grade 316LN stainless steel the following observation has been reported (cf. Obst, Nyilas, 1991; 1998): “it is evident that a substantial amount of martensite is generated only on

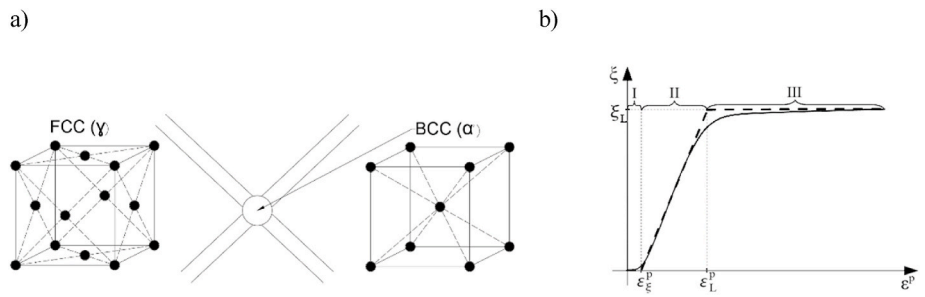


**Fig. 2.** (a) Illustration of the plastic strain induced fcc-bcc phase transformation: the fcc matrix and the martensitic (bcc) embryo at the shear bands intersection, (b) linearized kinetics of phase transformation expressed in terms of the volume fraction of secondary phase versus the plastic strain: I- low transformation rate, II- fast transformation, III- asymptotically vanishing transformation.

sections of uniform deformation and the martensite transformation $\gamma \rightarrow \alpha'$ virtually stops on the serrated sections". Apparently, there is substantial lack of systematic investigations related to the problem of coexistence of the serrated deformation and the phase transformation, and the above observation is based on the incidental results only. It is well known that the intermittent plastic flow, localized in the shear bands when stretching the samples in liquid helium, produces large amounts of stacking faults that might become potential nucleation sites of the secondary phase ($\alpha'$ martensite). Therefore, it is of primary importance to explain this problem, and to bring suitable evidence to the discussion focused on the coexistence of both phenomena.

In the next section, experimental evidence for coupling between the intermittent plastic flow (serrated yielding) and formation of the shear bands is explained. Moreover, propagation of the phase transformation front along the sample is measured, including the propagation velocity, and illustrated. In the subsequent section, the microstructure evolution across the shear band is analysed and strong evidence for the occurrence of the phase transformation inside the shear band is shown. Also, the crystallographic orientation of the grains in the course of martensitic transformation is illustrated.

### 3.1. Experimental evidence

Dedicated equipment was used to perform all necessary experiments (tests). It has been set to trace the onset and the propagation of the phase transformation during the intermittent plastic flow at constant temperature (LHe). The custom built experimental set-up consists of the cryostat equipped with the sample holder and multiple sensors, including the thermistors, the extensometers and the force transducers. The set-up is equipped with suitable thermal shields in order to reduce the heat transfer to the outside of the cryostat (Fig. 5). The cryostat with the insert is placed in the traction machine equipped with the force and the displacement control. Liquid helium was stored in a dedicated, vacuum insulated dewar. By increasing the pressure, the helium was transferred via dedicated transfer line directly to the cryostat, mounted between traction machine grips.

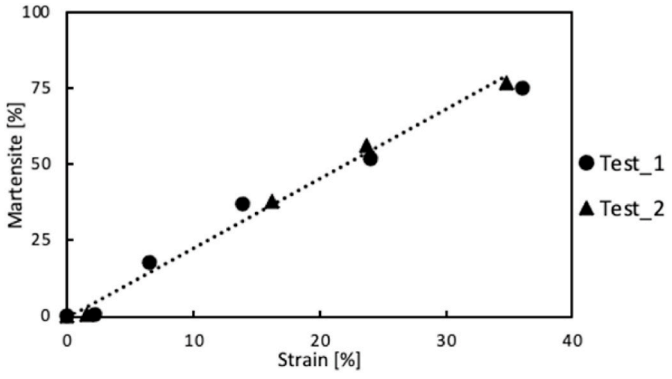


**Fig. 3.** Experimentally determined phase transformation kinetics for grade 316L at 4.2 K: linearized kinetics with lack of the phase transformation threshold, and maximum volume fraction of martensite reaching 77% at the strain of 35%.

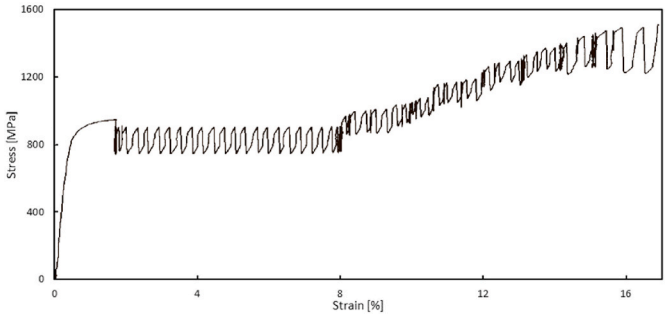


**Fig. 4.** Intermittent plastic flow consisting of two stages: regular (perfect, below 8% strain) and irregular (hardening, above 8% strain) for grade 316L stainless steel at 4.2 K: in the present paper the constitutive model is developed for the regular stage (stage 1) only.

The cryostat consists of two thin-walled stainless steel vessels, one inside the other, with the vacuum in-between in order to reduce the heat transfer by conduction. The copper thermal shields located in the cryostat reduce the heat transfer by limiting the convection and the radiation. Liquid helium is supplied to the cryostat by means of the transfer line, until the specimen is fully immersed in the medium. LHe level in the vessel is controlled by means of dedicated thermistor. Bottom of the external vessel is attached to the crosshead of the tensile test machine. The sample is loaded by means of a shaft connected to the upper frame of the machine. A set of selected transducers, suitable for extremely low temperatures, was used in the measurements. The elongation of the specimen was measured by means of special clip-on extensometers, symmetrically mounted on the specimen gauge length. The force was measured by dedicated piezoelectric transducer, mounted just behind the specimen – between the specimen and the loading rod. The reference set of instruments consists of the original force transducer integrated in the tensile test machine, and the LVDT transducer, both located outside the cryostat and supported by a separate data acquisition system. The quasistatic tests were performed with constant speed of the crosshead (displacement control) equal to 0.5 [mm/min].

Small dimensions of the cryostat necessitate application of special specimens. Flat, type dog bone specimens (Fig. 5b), made of grade 316L stainless steel, were used. The gauge length of the flat specimens was equal to 30 mm and had the cross-section of 1.5 mm × 2.0 mm. The samples were cut from the fine gauge stainless steel sheets by means of WEDM in two directions: parallel and perpendicular to the rolling direction. The chemical composition of grade 316L stainless steel, used to manufacture the samples, is presented in Table 1.

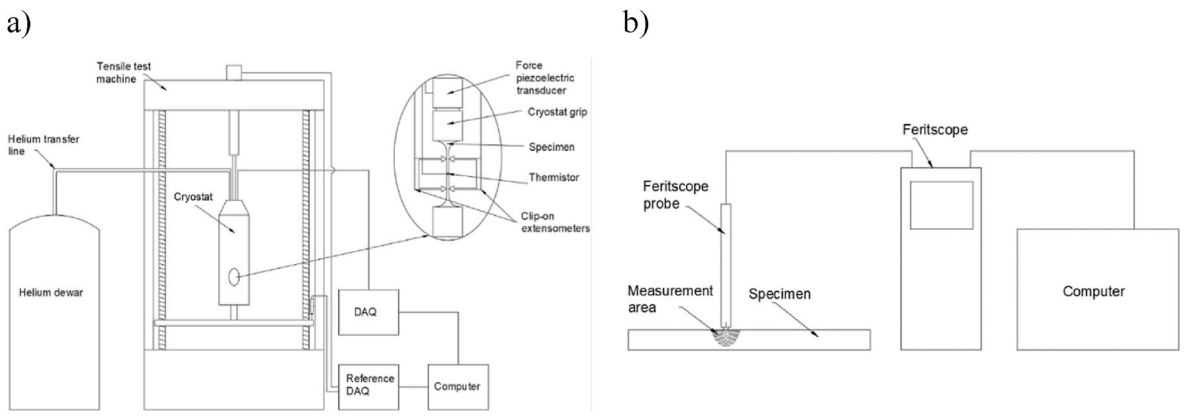


**Fig. 5.** Experimental set-up: (a) cryostat containing the insert with the sample and suitable instrumentation (extensometers, force transducer, thermistors, etc.) inside the traction machine, the helium transfer line and the data acquisition system, (b) the feritscope and the probe scanning the specimen in order to measure the average volume fraction of the secondary phase.

**Table 1**
Chemical composition of grade 316L stainless steel.

| Chemical composition (%) | | | | | | | |
|---|---|---|---|---|---|---|---|
| C | Si | Mn | P | S | Cr | Ni | N |
| ≤ 0.030 | 1.00 | 2.00 | 0.045 | 0.015 | 18.200 | 11.500 | – |

The volume fraction of the secondary phase was measured by means of the feritscope (Fig. 5b). The gauge length of the specimens was subdivided into 1 mm sections, each of them determined the measuring points of the volume fraction of the secondary phase. In the vicinity of the shear band, the volume fraction of martensite was measured within the sections of 0.2 [mm]. Small width and thickness of the specimens requires use of the correction factors in order to take into account the influence of edge proximity, the thickness and type of the ferromagnetic material. The shape correction factors were applied based on the correction curves provided by the manufacturer of the measuring device (feritscope). The correlation factor between the readout of the feritscope and the correct martensite content (the value of 1.7, based on Talonen et al., 2004), was applied. The volume fraction of martensite was estimated by means of the following formula:

$$\xi(\%) = \xi_{Fr}(\%) \bullet CF_T \bullet CF_E \bullet CM \tag{4}$$

where $\xi_{Fr}(\%)$ denotes the feritscope readout, and $CF_T, CF_E, CM$ are the correction factors. As the increase of the secondary phase is strongly correlated to the oscillatory mode of plastic deformation, the measurements were carried out after a predefined number of serrations. The maximum level of the volume fraction of martensite in the course of the regular stage of the stress oscillations (shear band "travelling" across the gauge length) is equal to 38%. The estimated propagation velocity of the phase transformation front, understood as the ratio of constantly increasing secondary phase bandwidth to time in which the phase transformation took place, is similar throughout the whole regular stage and equal to 0.07 [mm/s].

The measurement taken by the feritscope refers to the average value of the secondary phase content in a given volume, covered by the head of the instrument. Location of the phase transformation front is determined with the precision of the instrument, defined by the size of the head. In particular, the volume fraction of secondary phase after single serration is shown in Fig. 6. The maximum of 9% of secondary phase in the middle of the shear band was detected after the first serration. Next measurements were performed after predefined number of serrations (serration clusters). The propagation time of the phase transition front was defined as the time between the occurrence of the first and the last serration in the cluster.

The measurement of the phase transformation in the shear band narrower than the feritscope working field is affected by a measurement error. It is caused by averaging the readout of the ferromagnetic fraction over the area covered by the feritscope head. Knowing the shear bandwidth (l), the radius of the feritscope working range (r), and the sample width (g), the amount of martensite in a fairly narrow band can be

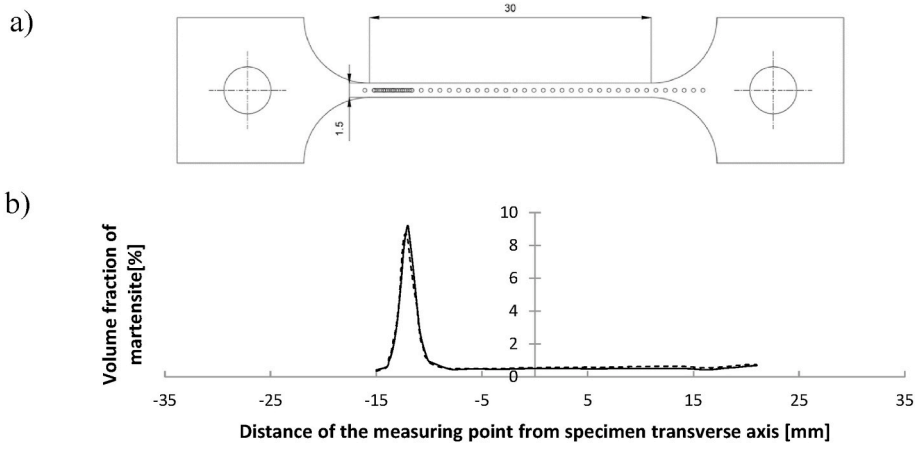


**Fig. 6.** (a) Localization of the measurement points (small circles) along the sample axis, (b) distribution of the volume of fraction of martensite after the first serration, corresponding to formation of the first shear band (the maximum volume fraction of martensite reaches 9%).

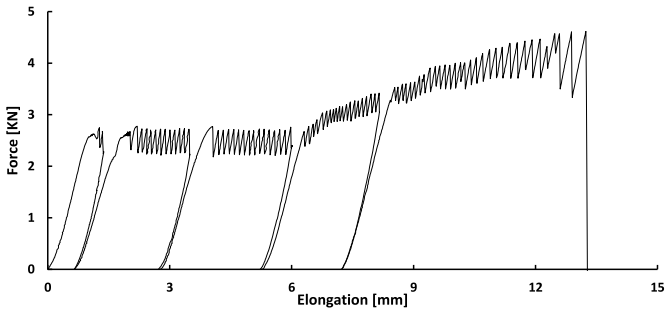


**Fig. 7.** Multiple loading-unloading of grade 316L stainless steel at 4.2 K in terms of force versus elongation, containing two stages: the regular and the irregular, and corresponding to the measurements of the volume fraction of martensite by means of the feritscope.

determined:

$$\xi(\%) = \xi_{measurement}(\%) \bullet \frac{\pi r^2 - 2\left(r^2 \arccos\left(\frac{g}{2r}\right) - \frac{g}{4}\sqrt{g^2 - 4r^2}\right)}{lg} \tag{5}$$

During the static tensile test, interrupted just before the first abrupt drop of stress, negligible volume fraction of ferromagnetic phase has been found, although rather significant plastic deformation occurred in the sample. This shows that an intensive fcc-bcc phase transformation takes place during the serration.

Generally, the campaign of tests has been focused on precise measurements of the initiation and the propagation of the shear bands, with the checkpoints set after the preselected serrations. The samples were tested according to a predefined program, comprising loading until the first, the second, the fourteenth and the twenty-ninth serration, the latter representing the complete loading until the whole gauge length was consumed (stage 1 of the intermittent plastic flow). As soon as the sample was loaded to the predefined stage, it was extracted from the cryostat and subjected to thorough microscopic analysis by means of the scanning electron microscope (SEM), including the crystallographic (EBSD) detector. Afterwards, the sample was subjected to the magnetometric measurements by means of the feritscope in order to detect the amount of secondary phase produced within the shear band. It is worth pointing out, that the experiments using liquid helium as the cryogenic medium are extremely complex and expensive. For this reason, the number of tests performed was limited to four, taking into account rather high reproducibility of the experimental data. The parameters of all four tests are presented in Table 2.

Even if each test was performed by means of a new sample of the same geometry, the results were repeatable. Also, the evolution of the microstructure as well as the amount of the secondary phase detected by means of the feritscope, were quite similar. The dashed line in Fig. 8 marks the values obtained by the measurements performed on the opposite face of the sample, which are nearly identical with the values obtained on the basic face (thus, the number of the measurements was doubled). The uncertainty of this method is rather small, and the measurement itself is repeatable due to the elimination of the human factor (semi-automatic process).

**Table 2**
The parameters of four tests performed in liquid helium (4.2 K).

| Number | Max. Load | Number of serrations | Temperature | Martensite fraction | Remarks |
|---|---|---|---|---|---|
| 1 | 2.67 kN | 1 | 4.2 K | 9% | partial |
| 2 | 2.67 kN | 2 | 4.2 K | 18% | partial |
| 3 | 2.73 kN | 14 | 4.2 K | 38% | partial |
| 4 | 2.73 kN | 29 | 4.2 K | 39% | complete |

In order to verify the presence of the secondary phase across the shear band, the microscopic observations were performed. Thanks to these observations, the microstructure of the material as well as the volume fraction of secondary phase (ε and α' martensite variants) were analysed at the edge and in the middle of shear band. As the scanning electron microscope (SEM) allows to perform local observations at the predefined points on the surface of the sample, the microstructure has been observed in very small regions of the stainless steel.

### 3.2. Microstructure and phase transformation

In the present Section, application of the backscattered electron diffraction method (EBSD) is discussed. The EBSD allows to accurately analyse the phase transformation in the crystallographic context. On the surface of the sample, 2 mm wide macroscopic shear band with deformed geometry was observed by means of the scanning electron microscope (SEM). The macroscopic shear band corresponds to the area of the ferromagnetic phase recorded during the measurements performed by using the feritscope. Based on these observations, three EBSD measurement sites were selected. The first measurement was made 2 mm away from the centre of the shear band, next 1 mm from the centre of the shear band, and the last one in the middle of the shear band.

The sample used was made of 316L stainless steel and presented originally nearly perfect austenitic structure. As a result of straining at the temperature of liquid helium (4.2 K), the plastic strain induced fcc-bcc phase transformation took place. The transformation consists essentially in the evolution of the crystal structure from the regular face-centred cubic austenite (fcc) to the regular body-centred cubic (bcc) martensite. However, the primary austenitic phase begins first to transform into a transition phase (martensite ε), characterized by the compact hexagonal lattice, and then into the martensite α', characterized by the spatially centred regular lattice. The analysis by means of the EBSD provided information on the percentage of the volume share of the phases at a given point, as well as a graphical visualization of the grains containing the phases (Figs. 9 and 10).

The secondary phase (α' martensite) is produced in a narrow 2 mm wide band, and occurs in stages. In the middle of the band, the largest volume fraction of secondary phase reaches some 6.4% (Fig. 9 a). When moving away from this point, the martensite content decreases, reaching some 4.6% at 1 mm from the centre (Fig. 9 b), and around 3.7% at a distance of 2 mm from the centre (Fig. 9 c).

Formation of twin boundaries can be observed at the macroscopic level in the form of very small stress oscillations in the stress-strain curve. The twins were also observed by means of the EBSD at each of the test sites, and are indicated in Fig. 10.

The austenite grains are in a specific crystallographic orientation that results from the processes which the sample was subjected to, i.e. rolling and stretching. The rolling induced the grains with the Brass orientation {1 1 0} <1 1 2>, and the uniaxial stretching process produced the Goss{1 1 0} <1 0 1>, Cu {1 1 2} <1 1 1> texture (Fig. 11). In the middle of the band, the Cu orientation dominates, which in turn has a tendency to twin, i.e. to shear. The shear is the precursors of the phase transformation resulting in formation of the epsilon martensite, and then the alpha martensite (Fig. 11a). At a distance of 2 mm from the centre of the band, the Goss orientation (marked with a circle) prevails, which means that the grain does not have a tendency to shear, but willingly deforms plastically (Fig. 11b).

## 4. Physically based multiscale constitutive model

The physically based constitutive model (Böhm, H., 1998; Ottosen, Ristinmaa, 2005) comprises essentially two features, corresponding directly to the phenomena observed in the proximity of absolute zero: the intermittent plastic flow (serrated yielding) and the plastic strain induced fcc-bcc phase transformation. The first phenomenon is rather

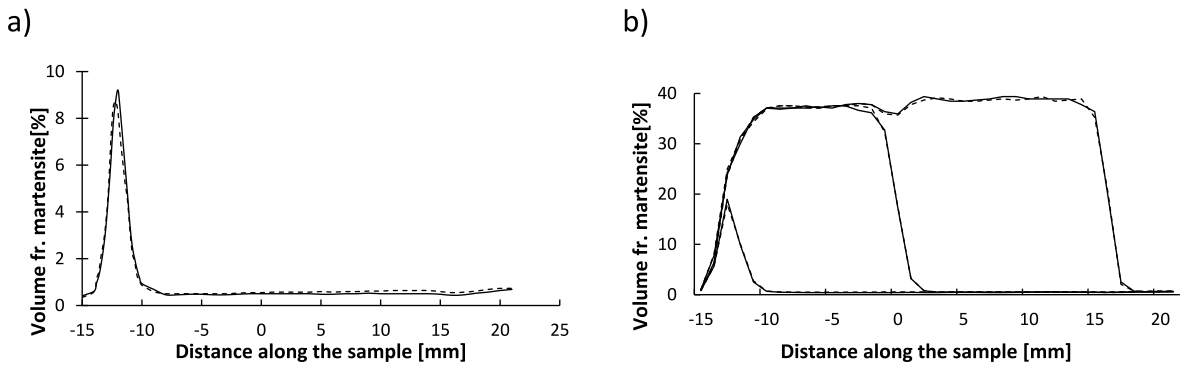


**Fig. 8.** (a) Volume fraction of martensite after single serration as a function of distance along the sample, (b) propagation of the phase transformation front during the regular stage of the intermittent plastic flow, registered after 2, 14 and 29 regular serrations.

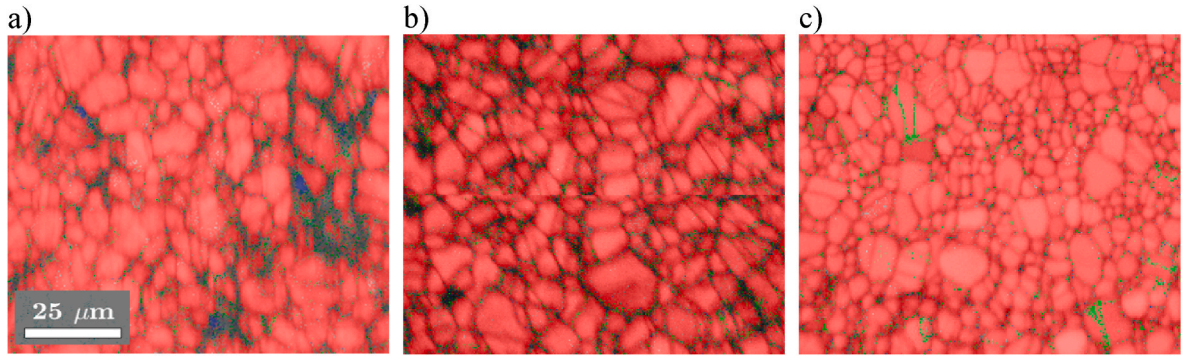


**Fig. 9.** Sample microstructure with marked grain boundaries and phase distribution: austenite (red), α′ martensite (green), ε martensite (blue): a) in the middle of the shear band, b) 1 mm from the centre of the shear band, and c) 2 mm from the centre of the shear band. (For interpretation of the references to colour in this figure legend, the reader is referred to the Web version of this article.)

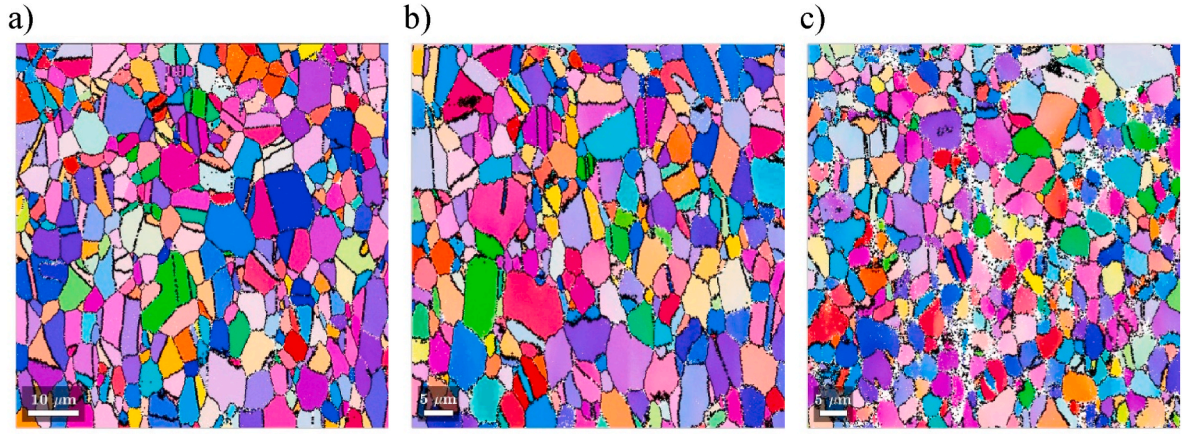


**Fig. 10.** Grain orientation with twin boundaries: a) in the middle of the shear band, b) 1 mm from the centre of the shear band, and c) 2 mm from the centre of the shear band.

complex as far as the constitutive and the numerical models are concerned. This is due to the fact, that each stress-strain oscillation (serration) is composed of four parts (Fig. 12 a): 1-elastic, 2-plastic flow with hardening, 3-drop of stress and 4-relaxation. As there is no unified mathematical formulation of all parts of the intermittent plastic flow, each part has to be modelled by means of separate set of the differential equations. For the first part, the classical linear isotropic elasticity is used. The second part is based on the rate independent plasticity, comprising mixed kinematic and isotropic hardening. The nonlinearity of hardening is directly associated with the plastic strain induced fcc-bcc phase transformation comprising two physical phenomena: the interaction of dislocations with the inclusions and the evolution of stiffness of two-phase continuum resulting from constantly changing proportions between the primary and the secondary phase. Both of them affect the tangent stiffness operator, that is computed at each stage of the deformation process. In order to trigger the serration (drop of stress), a parameter expressing the number of lattice barriers per unit surface (B) has to be computed. As soon as the number of lattice barriers per unit surface reaches a critical value (threshold function), the serration is triggered and the drop of stress takes place. The drop of stress is modelled in the form of a macroscopic slip, which means that two portions of lattice slide with respect to each other by a macroscopic

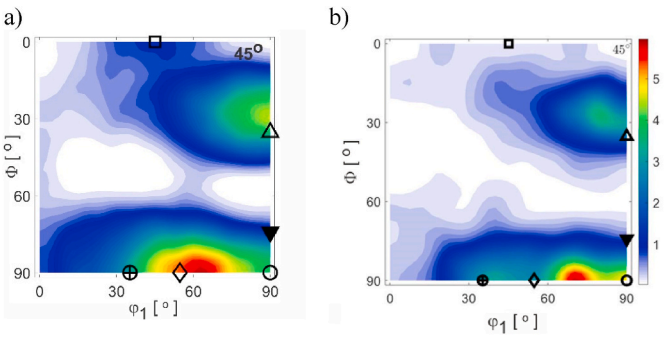


**Fig. 11.** ODF with marked orientations: Brass (rhombus), Goss (circle), Cu (triangle), Goss-Brass (circle with cross), Cu-Twin (rotated triangle). The function values constitute the multiples of a random misorientation (rdm).

value. As the macroscopic slip is compensated by the elastic unloading of both sliding portions of the lattice, the drop of stress occurs at a constant total strain. Given the value of the drop of stress, determined by the position of the yield surface with respect to the recovery surface, the amount of the macroscopic slip can be computed. Finally, if the amount of thermal energy stored in the lattice during the macroscopic slip is sufficient, the relaxation of stress takes place, and the serration is completed.

The most complex part of the model is related to the plastic flow (Tandon, G.P. and Weng, G.J., 1988), accompanied by the phase transformation driven hardening (Fig. 12a: 2-hardening). It is due to the fact, that the plastic strain induced fcc-bcc phase transformation introduces two types of nonlinearities into the hardening mechanism (Fig. 12b): the interaction of dislocations with the inclusions of the secondary phase, and the evolution of the overall stiffness of two-phase continuum. In order to take the latter into account a homogenization scheme has to be applied. Among different homogenization algorithms applied to model the behaviour of the heterogeneous materials, the Hill self-consistent implicit algorithm, the Mori-Tanaka (M-T) explicit algorithm as well as the periodic homogenization with the asymptotic expansion (cf. Préve et al., 2021) are well known. In the present model the Mori-Tanaka homogenization scheme is applied. The reason to use the M-T scheme is related to the fact, that in order to compute the tangent stiffness operator at each stage of the deformation process, the homogenization algorithm is repeated at each load step. Thus, the Mori-Tanaka explicit algorithm is more convenient. In the present model, a novel formulation based on two surfaces: the yield surface and the recovery surface (Fig. 13a), has been introduced. Such a formulation is consistent with the observation related to the first stage of the intermittent plastic flow, where the regular serrations take place between two constant stress levels (Figs. 4 and 7). The constitutive model is described in detail in Sections 3.1 through 3.4, including new formulation of the intermittent plastic flow based on double surface model, and the plastic strain induced fcc-bcc phase transformation model, comprising the micromechanics and the homogenization based nonlinear hardening.

It is worth pointing out, that the constitutive model is for the first time developed for the local coordinate system, associated with the orientation of the shear band with respect to the global coordinates (Fig. 14). The analysis is performed inside the shear band, as long as it is

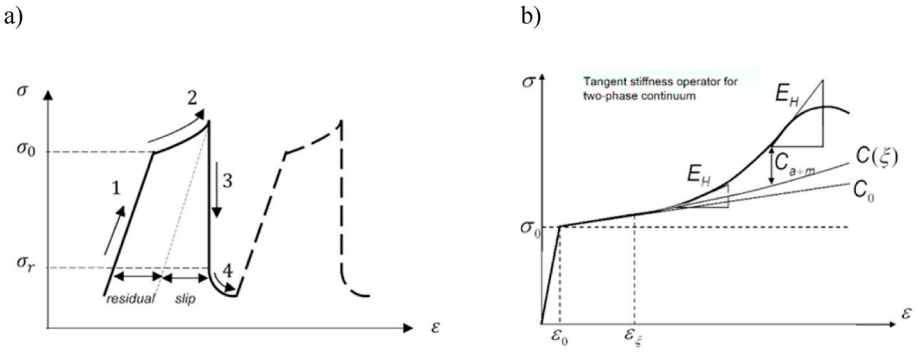


**Fig. 12.** (a) Single serration during the regular stage of loading (1-elastic, 2-hardening, 3-drop of stress, 4-relaxation); (b) tangent stiffness operator of two-phase continuum: $C_0$, $C$, $C_{a+m}$ denote the hardening moduli: initial (pure austenitic matrix), micromechanics based (interaction of dislocations with the inclusions), and homogenization based (evolution of the proportion between the phases), respectively.

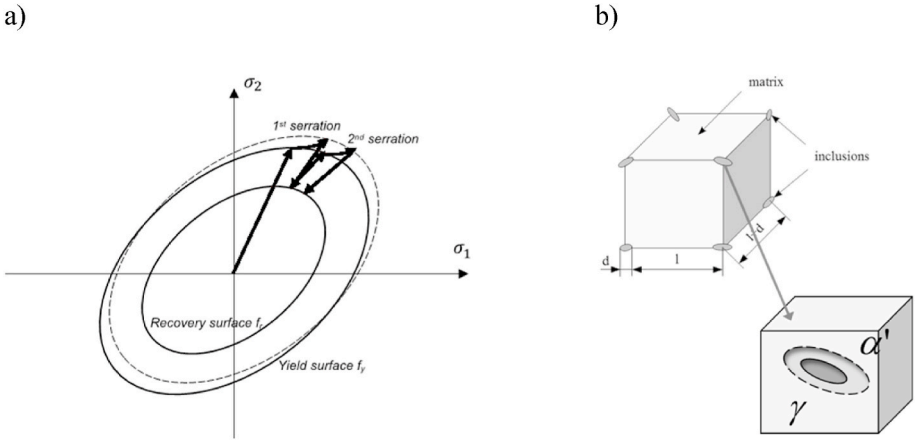


**Fig. 13.** (a) New double surface model of the regular stage of the IPF, including the yield and the recovery surfaces – illustration of two subsequent serrations, (b) type Eshelby ellipsoidal inclusion of the secondary phase (martensite) in the austenitic matrix (generation of the phase transformation strain).

active, and the local state of stress is correlated with the global state of stress defined for the whole sample (transformation). Thus, the constitutive model is developed in the RVE located inside the active shear band, and as soon as the shear band becomes passive (is "blocked" by the secondary phase) and a new shear band is formed in its proximity, the RVE is moved to the new, active shear band and the analysis is repeated. Such a sequential formulation allows to correlate each serration with the corresponding shear band, and obtain simultaneously the local and the global state of the stress. As the whole process is kinematically controlled, the position of each shear band is determined with respect to the global coordinate system. For this reason, the number of serrations corresponds to the number of shear bands during the regular stage of the IPF. This approach is based on the assumption that the intermittent plastic flow, accompanied by the phase transformation, is localized inside the active shear band, and the rest of the sample being passive, forms the boundary conditions for the local process.

### 4.1. Intermittent plastic flow – regular stage

In the present chapter regular serrations, corresponding to the stress oscillations between the lower bound and the upper bound in the stress-strain curve (Fig. 4), are modelled. It is assumed that the regular serrations occur in the small or moderately small strains range (below 10%), therefore the Cauchy and the Hencky strain measures do not substantially differ (by less than 5%). Thus, the small strains approach is fully justified. The model essentially reflects the smooth plastic flow in the active shear band during the serration (Fig. 13a, 2-hardening), and production of the lattice barriers, as well as accumulation of the dislocations on the barriers in the form of the pile ups. At each stage of this process, the surface density of lattice barriers B is checked in the context of the drop of stress criterion. As soon as the serration criterion is reached, the drop of stress takes place, and the amount of the macroscopic slip is computed (Fig. 13a, 3-drop of stress). The drop of stress occurs under the condition of constant total strain, and its depth is limited by the recovery surface, as illustrated in Fig. 14a. The constitutive model of the IPF begins with the kinetics of formation of the lattice barriers within the shear band. Here, the function $B$ reflects surface density of the pile-ups of dislocations at the internal lattice barriers. The driving force remains the cumulative plastic strain (the Odqvist parameter $p$):

$$B_{,t} = F_{\mathrm{B}}^{+}\left(\rho, T, \sigma_{ij}\right) p_{,t} H(p - p_{\mathrm{B}}) \tag{6}$$

The function $F_{\mathrm{B}}^{+}$ depends on the dislocation density $\rho$, the temperature $T$ and the state of stress $\sigma_{ij}$. The threshold function $H$ has been introduced in order to set the threshold $p_{\mathrm{B}}$ for the formation of the lattice barriers. The cumulative plastic strain is expressed by:

$$p = \int_0^{\widetilde{t}} \left(\varepsilon_i^p\right)_{,t} dt \quad ; \quad \left(\varepsilon_i^p\right)_{,t} = \sqrt{\frac{2}{3}\left(e_{ij}^p\right)_{,t}\left(e_{ij}^p\right)_{,t}} \tag{7}$$

where $\left(e_{ij}^p\right)_{,t}$ is the deviatoric plastic strain rate (the incompressibility has been assumed). The evolution of dislocations density $\rho$ is described by the following equation (Kocks and Mecking, 2003; Ma et al., 2006):

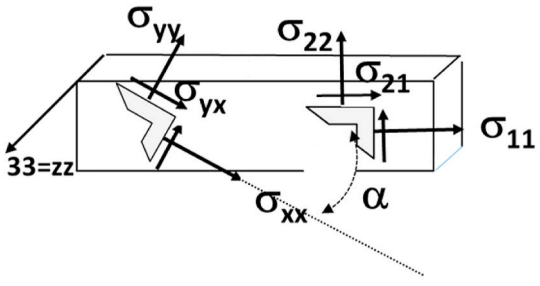


**Fig. 14.** Transformation of stresses: the state of stress in the sample (1, 2, 3), and the state of stress in the shear band (x, y, z).

$$\rho_{,\gamma} = \left(\rho_{,\gamma}\right)^{+} + \left(\rho_{,\gamma}\right)^{-} \tag{8}$$

where $\gamma$ denotes the shear strain. Production $(..)^{+}$ and annihilation $(..)^{-}$ of dislocations are expressed by:

$$\left(\rho_{,\gamma}\right)^{+} = (\widetilde{\lambda} b)^{-1}, \left(\rho_{,\gamma}\right)^{-} = -k_{\mathrm{a}}\rho \tag{9}$$

where $\widetilde{\lambda}$ denotes the mean free path of dislocation, $b$ is the Burgers vector and $k_{\mathrm{a}}$ is the dislocation annihilation constant. The mean free path of dislocations reads:

$$\widetilde{\lambda}^{-1} = d^{-1} + k_1\sqrt{\rho} \tag{10}$$

where $d$ denotes the average grain size, whereas, $k_1$ is a constant. Finally, one obtains:

$$\rho_{,\gamma} = (db)^{-1} + k_1\sqrt{\rho} b^{-1} - k_{\mathrm{a}}\rho \tag{11}$$

The meso-macro transition involves the Taylor factor $M$:

$$\sigma = M\tau, \varepsilon = M^{-1}\gamma \tag{12}$$

Neglecting the elastic strains, one obtains:

$$\rho_{,p} = M\left[(db)^{-1} + k_1\sqrt{\rho}\, b^{-1} - k_a\rho\right] \tag{13}$$

where $p$ is the cumulative plastic strain. The average shear stress in the lattice reads:

$$\tau_{av} = \tau_0 + \mu\alpha b\sqrt{\rho} \tag{14}$$

where $\mu$ denotes the shear modulus, and $\alpha$ is the dislocations interaction factor. The shear stress at the head of dislocation pile-up amounts to:

$$\tau_e = \pi(1-\nu)(\mu b)^{-1}\overline{\Lambda}\tau_{av}^2 \tag{15}$$

The mean free path of dislocation $\overline{\Lambda}$ comprises three types of obstacles: the grain boundaries ($d$), the dislocations ($\rho$), and the lattice barriers ($B$):

$$(\overline{\Lambda})^{-1} = d^{-1} + k_1\sqrt{\rho} + k_2\sqrt{B} \tag{16}$$

It is assumed that the failure of the lattice barriers is determined by the pair of variables $(B, \tau_e)$, comprising the surface density of dislocation pile-ups at the lattice barriers and the average shear stress at the head of dislocation pile-up. In order to trigger drop of stress (serration), the following conditions have to be fulfilled:

$$\begin{aligned} &\tau_{\mathrm{e}} \le \tau_{\min}; \quad B = B_{\mathrm{cr}} \quad ; \quad B \le B_{\min}; \quad \tau_{\mathrm{e}} = \tau_{\mathrm{cr}} \quad ; \quad \tau_e > \tau_{\min} \\ &\wedge B > B_{\min}; \quad F(B, \tau_e) = 0 \end{aligned} \tag{17}$$

with function $F$ expressed in a linear form:

$$F(B, \tau_{\mathrm{e}}) = (B - B_{\min})(\tau_{\min} - \tau_{\mathrm{cr}}) - (B_{\mathrm{cr}} - B_{\min})(\tau_{\mathrm{e}} - \tau_{\mathrm{cr}}) \tag{18}$$

and the following supplementary conditions:

$$B_{\min}/B_{\mathrm{cr}} = \alpha_{\mathrm{B}} \quad ; \quad \tau_{\min}/\tau_{\mathrm{cr}} = \alpha_\tau \tag{19}$$

For the multiaxial loads the drop of stress is apportioned to the principal stress directions:

$$\frac{\Delta\sigma_J^{\mathrm{serr}}}{\Delta\sigma_K^{\mathrm{serr}}} = \frac{\sigma_J}{\sigma_K}\ ; \ J, K = 1, 2, 3 \quad \text{and} \quad J \ne K \tag{20}$$

and each serration is accompanied by the macroscopic slip of the following magnitude (unloading of both sliding portions of the lattice):

$$\Delta\varepsilon_I^{\mathrm{p,serr}} = -\frac{1}{E}\left[\Delta\sigma_I^{\mathrm{serr}} - \nu\left(\Delta\sigma_J^{\mathrm{serr}} + \Delta\sigma_K^{\mathrm{serr}}\right)\right] \tag{21}$$

Thus, within single serration corresponding to an active shear band two types of plastic flow take place: the redistributed motion of dislocations in the lattice, and the macroscopic slip within the shear band. As each serration generated during the regular stage of the IPF occurs – for the uniaxial process – between the lower and the upper bound of the stress, it is necessary to convert these bounds to the multiaxial state of stress. It can be done by means of the yield surface for the plastically active part of the process, and by means of the predefined recovery surface, corresponding to the lower bound of the stress. The recovery surface constitutes some sort of rebound surface, where each new serration is initiated. This concept corresponds to the multi-surface plasticity models, well known in the constitutive modelling. Moreover, regularity of the initial stage of the IPF suggests that the recovery surface should be expressed by a regular shape, similar to the yield surface. Such a model is developed in the next section.

### 4.2. Double surface model in plasticity

In order to describe single serration corresponding to an active shear band, new double surface model has been developed within the rate independent plasticity. It has been assumed that the plastic flow begins as soon as the yield surface is reached, and persists until the serration criterion (Eq. (17)) is fulfilled. When the serration criterion is satisfied the drop of stress corresponding to the macroscopic slip takes place. The stress state "drops" from the yield surface to the recovery surface, where the next serration begins. Thus, the steps 2 and 3 indicated in Fig. 12a occur between the yield surface and the recovery surface, as demonstrated in Fig. 13a. Both forms of the inelastic deformation, i.e. the smooth motion of dislocations and the macroscopic slip, are essentially accommodated in the model.

In particular, the smooth plastic flow obeys the classical rate independent plasticity:

$$\sigma_{ij} = E_{ijkl}(\varepsilon_{kl} - \varepsilon^{p}_{kl}) \tag{22}$$

During the regular stage of serrations, the yield function takes the following form:

$$f_y(\sigma_{ij}, X_{ij}, R) = \sigma_i - \sigma_y - R \quad ; \quad \sigma_i = \sqrt{\frac{3}{2}(s_{ij} - X_{ij})(s_{ij} - X_{ij})} \tag{23}$$

where $\sigma_y$, $R$ denote the yield stress and the isotropic hardening variable, whereas, $s_{ij}, X_{ij}$ are the deviatoric stress and the back stress, respectively. The following yield and consistency conditions are used:

$$f_y(\sigma_{ij}, X_{ij}, R) = 0 \quad ; \quad df_y = 0 \tag{24}$$

For the classical (smooth) plastic flow, the associated flow rule is applied:

$$\left(\varepsilon^{p}_{ij}\right)_{,t} = \lambda_{,t}\left(f_y\right)_{,\sigma_{ij}} \tag{25}$$

where $\lambda$ denotes a time-like parameter. Hardening model comprises the kinematic and the isotropic hardening:

$$\left(X_{ij}\right)_{,t} = \frac{2}{3}C_X\left(\varepsilon^{p}_{ij}\right)_{,t} \quad ; \quad R_{,t} = C_R p_{,t} \tag{26}$$

where $X_{ij}$ is the back stress tensor, R is the isotropic hardening parameter, and $C_X, C_R$ denote the kinematic and the isotropic hardening moduli, respectively. The pair of variables $(B, \tau_e)$ is computed at every stage of single serration, and as soon as the criterion of the drop of stress is fulfilled, the macroscopic slip takes place. The drop of stress occurs at a constant total strain and lasts until the recovery surface is reached. The recovery surface (Fig. 13a) is defined in the following regular way, corresponding to the shape of the yield surface:

$$f_r(\sigma_{ij}) = \sigma_i - \sigma_r \quad ; \quad \sigma_i = \sqrt{\frac{3}{2}s_{ij}s_{ij}} \tag{27}$$

where $\sigma_r$ denotes its size that remains constant throughout the whole process.

It is worth underlining, that the amount of the macroscopic slip during single serration corresponds to the elastic unloading of two sliding portions of the continuum. In order to define motion of the yield surface in the course of serration, the evolution laws for the back stress and for the isotropic hardening parameter (Eq. (26)) have to be developed. As during each serration certain amount of the secondary phase is produced inside the active shear band, and the proportions between the phases are constantly evolving, it is necessary to take into account two mechanisms: the interaction of dislocations with the inclusions and the evolution of stiffness of two-phase continuum. Both of them affect mixed hardening, making the hardening laws highly nonlinear. The hardening model, defined for the local conditions inside the active shear band, is developed in the next sections.

### 4.3. Plastic strain induced fcc-bcc phase transformation

During the smooth part of each serration (Fig. 12a, 2-hardening), the plastic strain induced fcc-bcc phase transformation takes place inside the active shear band. Initially single-phase continuum (austenitic matrix) is replaced by two-phase continuum, composed of the austenitic matrix and the martensitic inclusions. The phase transformation substantially affects hardening, comprising essentially two physical mechanisms: he interaction of dislocations with the inclusions and the evolution of the macroscopic stiffness of two-phase continuum due to the increasing amount of the secondary phase. Both contributions are important for the overall behaviour of two-phase continuum, and for the stress level corresponding to given strain. Thus, mixed hardening becomes nonlinear and affects production of the lattice barriers within single serration. Modelling the plastic strain induced fcc-bcc phase transformation begins with the kinetics, that takes the linear form expressed in Eq. (2), and is backed by the experimental data shown in Fig. 3. Next, the general constitutive law, including the plastic strain $\varepsilon^{p}_{kl}$ and the phase transformation strain $\varepsilon^{bs}_{kl}$, is formulated:

$$\sigma_{ij} = E_{ijkl}\left(\varepsilon_{kl} - \varepsilon^{p}_{kl} - \varepsilon^{bs}_{kl}\right) \tag{28}$$

The mesoscopic phase transformation strain $\varepsilon^{bs}_{kl}$ has been obtained by integrating the microscopic eigen-strain tensor $\varepsilon^{bs}_{kl_\mu}$ over the RVE. Assuming approximately random orientation of the martensite inclusions, one obtains isotropic tensor of the following form:

$$\varepsilon^{bs}_{kl} = \frac{1}{3}\xi\Delta v I_{kl} \tag{29}$$

where $\Delta v$ denotes the volume change during the phase transformation, and $I_{kl}$ is the unit tensor. The 4th rank elasticity tensor can be decomposed in the following way:

$$E_{ijkl} = 3kJ_{ijkl} + 2\mu K_{ijkl} \tag{30}$$

where the tensors $J_{ijkl}$ and $K_{ijkl}$ are the volumetric and the deviatoric 4th rank projectors, respectively:

$$J_{ijkl} = \frac{1}{3}\delta_{ij}\delta_{kl}, I_{ijkl} = \frac{1}{2}\left(\delta_{ik}\delta_{jl} + \delta_{il}\delta_{jk}\right), K_{ijkl} = I_{ijkl} - J_{ijkl} \tag{31}$$

Here, $\delta_{ij}$ is the Kronecker symbol, and $k, \mu$ denote the bulk and the shear moduli, respectively. The plastic strain is obtained from Eq. (25), and the hardening takes the form that depends on the volume fraction of the secondary phase:

$$\left(X_{ij}\right)_{,t} = \frac{2}{3}C_X\left(\varepsilon^{p}_{ij}\right) = \frac{2}{3}g\left(\xi\right)\left(\varepsilon^{p}_{ij}\right)_{,t} \quad ; \quad R_{,t} = C_R p_{,t} = f(\xi)p_{,t} \tag{32}$$

The kinematic hardening variable (the back stress) is decomposed into two fractions:

$$\left(X_{ij}\right)_{,t}=\left(X_{ij}\right)_{,t}+\left(X_{ij}\right)_{,t}=\frac{2}{3}C(\xi)\left(\varepsilon_{ij}^{p}\right)+\frac{2}{3}G(\xi)\left(\varepsilon_{ij}^{p}\right)=\frac{2}{3}g(\xi)\left(\varepsilon_{ij}^{p}\right)_{,t} \tag{33}$$

that correspond to the behaviour of the austenitic phase in the presence of the localized small inclusions (interaction of dislocations with the inclusions, including the Orowan mechanism), and to the combination of the austenite and the martensite (increasing stiffness of two-phase continuum, based on the homogenization algorithm), respectively. Both effects are described in the next Sections 4.4 and 4.5.

### 4.4. Micromechanics based nonlinear hardening

When a dislocation meets an inclusion of average size $d$, much smaller than the average distance between the inclusions ($d \ll l$), a significantly higher shear stress is needed to overcome the obstacle. It has been demonstrated, that the shear stress needed for a dislocation to pass across the inclusion (the Orowan mechanism, cf. Sitko et al., 2010) is function of the volume fraction of martensite:

$$\tau_p=\frac{\mu b}{d}\sqrt[3]{\frac{6\xi}{\pi}} \tag{34}$$

Final expression for the shear stress reads:

$$\tau_p=\frac{\mu b}{d}\sqrt[3]{\frac{6\xi_0}{\pi}}\left(1+\frac{\Delta\xi}{3\xi_0}\right),\ \Delta\xi=\xi-\xi_0 \tag{35}$$

where $\mu$ denotes the shear modulus of the austenite, $b$ is the Burgers vector, and $\xi_0$ stands for the initial volume fraction of inclusions. The above is reflected by a correction function implemented in the back stress evolution law and imposed on the hardening modulus in the following form:

$$\chi(\xi)=1+h\xi \tag{36}$$

where $h$ is a material dependent parameter. The evolution law for the austenitic matrix containing the martensitic inclusions reads:

$$\left(X_{ij}\right)_{,t}=\frac{2}{3}C(\xi)\left(\varepsilon_{ij}^{p}\right)=\frac{2}{3}C_{a0}(1+h\xi)\left(\varepsilon_{ij}^{p}\right)_{,t} \tag{37}$$

where $C_{a0}$ denotes the hardening modulus of the original non-transformed austenitic phase.

### 4.5. Tangent stiffness of two-phase continuum

The increased stiffness of mixture of the parent and the product phases can be estimated by means of the mean field techniques (Ortolano González, et al, 2013). The Mori-Tanaka homogenization belongs to the techniques that can be applied to two-phase continuum, consisting of the elastic-plastic matrix (austenite) and the elastic inclusions (martensite). This technique is usually applied on the step-by-step basis, in order to obtain an updated tangent stiffness operator at each load step (Doghri, I. and Ouaar, A., 2003). As the austenitic matrix is elastic-plastic, the tangent stiffness operator is complex, nonlinear, and takes the form of 4th order tensor (Pierard, O. and Doghri, I., 2006). Thus, the stress increment can be calculated as:

$$\Delta\sigma_{ij}=E_{ijkl_{ta}}\Delta\varepsilon_{kl} \tag{38}$$

where $E_{ijkl_{ta}}$ is the 4th order tangent stiffness tensor, expressed in the following way:

$$E_{ijkl_{ta}}=3k_{ta}J_{ijkl}+2\mu_{ta}\left(K_{ijkl}-\frac{n_{rs}\otimes n_{rs}}{1+\frac{C}{3\mu}}\right) \tag{39}$$

and $n_{rs}$ is the tensor normal to the yield surface. It has been demonstrated (Sitko et al., 2010), that it is more convenient to reduce the tangent stiffness operator to its isotropic form (Chaboche and Kanouté, 2003), by performing a projection to the space of isotropic operators:

$$E_{ijkl_{ta}}=3k_{ta}J_{ijkl}+2\mu_{ta}K_{ijkl} \tag{40}$$

where:

$$k_{ta}=\frac{E_{ta}(\xi)}{3(1-2\nu_a)},\mu_{ta}=\frac{E_{ta}(\xi)}{2(1+\nu_a)},E_{ta}(\xi)=\frac{E_aC(\xi)}{E_a+C(\xi)} \tag{41}$$

and $E_a,\nu_a$ are the elasticity modulus and the Poisson ratio of the austenite, respectively. For what concerns the secondary phase, type Eshelby ellipsoidal and elastic inclusions are considered, therefore, the following elastic 4th order stiffness tensor is applied:

$$\Delta\sigma_{ij}=E_{ijkl_m}\Delta\varepsilon_{kl},E_{ijkl_m}=3k_mJ_{ijkl}+2\mu_mK_{ijkl} \tag{42}$$

where:

$$k_m=\frac{E_m}{3(1-2\nu_m)},\mu_m=\frac{E_m}{2(1+\nu_m)} \tag{43}$$

Here, $k_m,\mu_m$ are the bulk and the shear moduli of the martensite, respectively. Both stiffness tensors contribute to the resultant tangent stiffness operator, obtained for two-phase continuum by means of the Mori-Tanaka homogenization:

$$E_{ijkl_H}=E_{ijkl_{MT}}=3k_{MT}J_{ijkl}+2\mu_{MT}K_{ijkl} \tag{44}$$

Given the general principle of the mean field approach:

$$\left(E_{ijkl_{MT}}+E_{ijkl}^{*}\right)^{-1}=\sum_{r=a,m}f_r\left(E_{ijkl_r}+E_{ijkl}^{*}\right)^{-1} \tag{45}$$

where $f_r$ is the volume fraction of the constituent "$r$" ($a$ - for austenite, $m$ - for martensite), and $E_{ijkl}^{*}$ stands for the Hill influence tensor, the resultant stiffness tensor is obtained. The bulk and the shear moduli of two-phase continuum are computed from:

$$3k_{MT}+3k^{*}=\left(\frac{1-\xi}{3(k_{ta}+k^{*})}+\frac{\xi}{3(k_m+k^{*})}\right)^{-1} \tag{46}$$

$$2\mu_{MT}+2\mu^{*}=\left(\frac{1-\xi}{2(\mu_{ta}+\mu^{*})}+\frac{\xi}{2(\mu_m+\mu^{*})}\right)^{-1} \tag{47}$$

$$k^{*}=\frac{4}{3}\mu_{ta},2\mu^{*}=\frac{\mu_{ta}(9k_{ta}+8\mu_{ta})}{3(k_{ta}+2\mu_{ta})} \tag{48}$$

As the stress increment has been essentially decomposed into two fractions:

$$\Delta\sigma_{ij}=\Delta\sigma_{ij_a}+\Delta\sigma_{ij_{a+m}}=E_{ijkl_{ta}}\Delta\varepsilon_{kl}+\left(E_{ijkl_H}-E_{ijkl_{ta}}\right)\Delta\varepsilon_{kl} \tag{49}$$

and

$$\Delta\sigma_{ij_{a+m}}=\left(E_{ijkl_H}-E_{ijkl_{ta}}\right)\Delta\varepsilon_{kl}^{p},\Delta\varepsilon_{kl}\approx\Delta\varepsilon_{kl}^{p} \tag{50}$$

the surplus stress increment, representing the coexistence of both phases, can be obtained:

$$\Delta\sigma_{ij_{a+m}}=2(\mu_{MT}-\mu_{ta})\Delta\varepsilon_{ij}^{p}=C_{a+m}\Delta\varepsilon_{ij}^{p},\Delta\varepsilon_{kl}\approx\Delta\varepsilon_{kl}^{p} \tag{51}$$

where $C_{a+m}$ denotes the surplus tangent stiffness modulus. Given the Bauschinger parameter $\beta$, the surplus stress increment can be apportioned to the evolution laws for the back-stress and for the isotropic hardening parameter, respectively:

$$\left(X_{ij}\right)_{,t}=\beta\frac{2}{3}C_{a+m}\left(\varepsilon_{ij}^{p}\right)\quad;\quad R_{,t}=(1-\beta)C_{a+m}p_{,t} \tag{52}$$

Finally, the evolution laws, including the interaction of dislocations with the inclusions and the increased stiffness due to the mixture of both phases, read:

$$\left(X_{ij}\right)_{,t}=\frac{2}{3}\left[C(\xi)+\beta C_{a+m}(\xi)\right]\left(\varepsilon_{ij}^{p}\right)_{,t}=\frac{2}{3}\,C_X\left(\varepsilon_{ij}^{p}\right)_{,t} \tag{53}$$

$$R_{,t}=(1-\beta)C_{a+m}(\xi)p_{,t}=C_R p_{,t} \tag{54}$$

The above nonlinear hardening affects significantly the stress distribution in an active shear band.

## 5. Numerical simulations

Analytical integration of the above presented constitutive law is hardly possible, hence, the numerical approach has been implemented. Fig. 14 explains the notation used for stress and strain directions (1, 2, 3) in the sample, as well as in the shear band (x, y, z) rotated by $\alpha$ with respect to the principal directions. For the uniaxial tension $\sigma_{11} > 0$, whereas $\sigma_{22} = \sigma_{33} = 0$, and $\varepsilon_{11} > 0$ whereas $\varepsilon_{22} = \varepsilon_{33} < 0$.

Three-dimensional formulation has been developed in order to make it useful for more complex loading programs, e.g. two or three directional loads. Thus, the out-of-plane stress component $\sigma_{zz} = \sigma_{33}$ is explicitly included in the physical relations, the increment of the plastic strain in this direction $\Delta\varepsilon_{zz}^{p}$ is derived from the associated flow rule, and the total strain increments in the directions normal to tension $\Delta\varepsilon_{22}$ i$\Delta\varepsilon_{33}$ are iterated (in the plastic deformation range), so as to satisfy the equilibrium conditions $\sigma_{22} = 0$ and $\sigma_{33} = 0$. The numerical algorithm and the values of the parameters adopted for the numerical analysis are presented in Annex I.

The numerical results are illustrated by means of the stress and the strain components in the shear band. There is only one non-zero stress component $\sigma_{11}$ in the sample, related to the principal direction (tension direction). If $\alpha = 45^{\circ}$, the directions $x$ and $y$ in the shear band are indistinguishable, hence $\sigma_{xx} = \sigma_{yy} = \sigma_{xy}$, $\varepsilon_{xx} = \varepsilon_{yy}$. For $\alpha = 40^{\circ}$ one deals with three various stress components in the shear band (Fig. 15c).

The above results correlate well with the experimental data

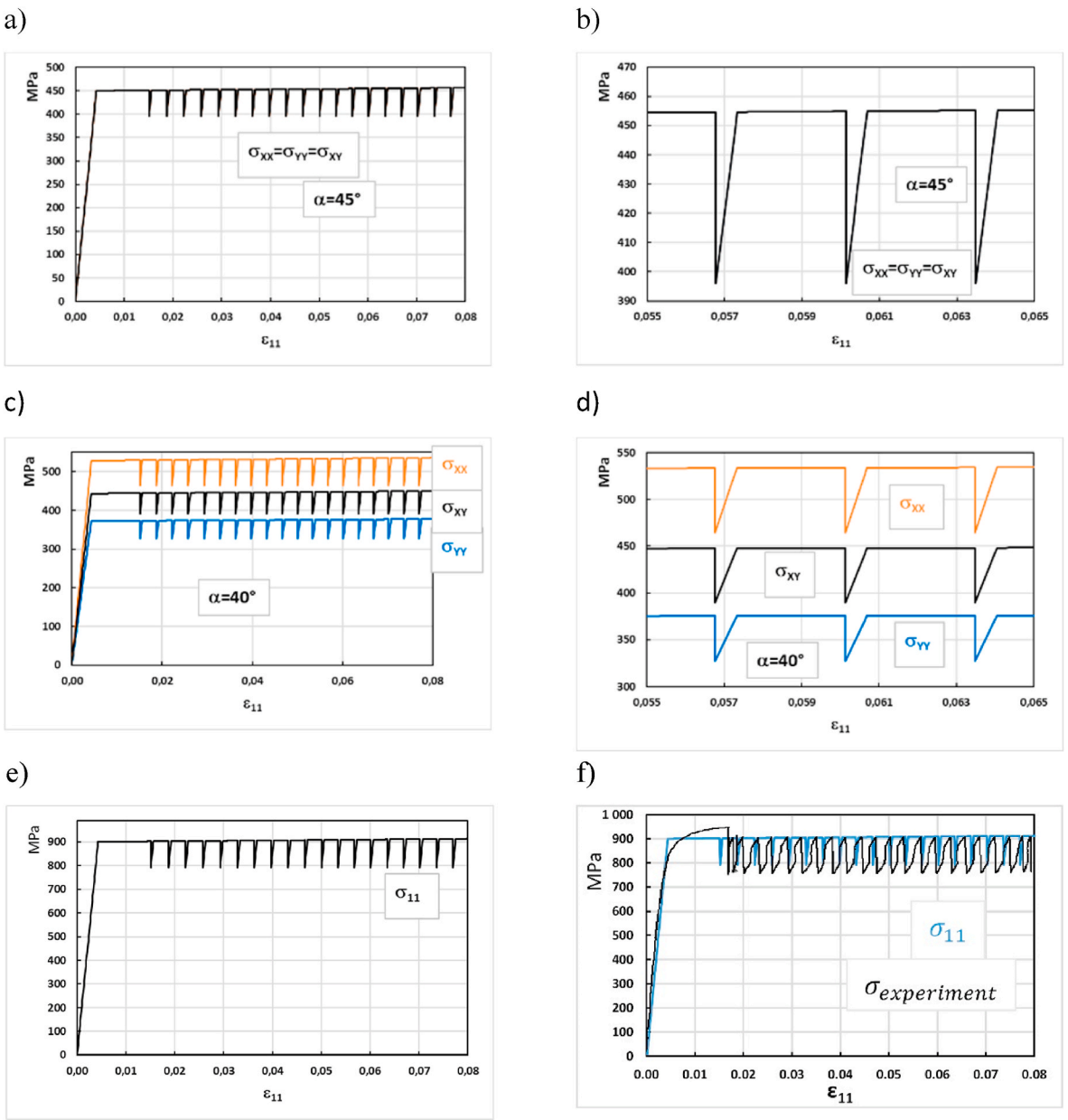


**Fig. 15.** Stress components in the shear band (a, b, c, d) and in the tension direction (e) as functions of the principal strain (tension); α - angle of rotation of the shear band with respect to the tension direction (principal stress in tension direction $\sigma_{11}$ is invariant with respect to α); (f) correlation between the numerical simulation and the experimental data.

presented in Chapter 2, both in terms of the amplitude and the frequency of serrations. In particular, the stress oscillations shown in Fig. 15e clearly demonstrate the amplitude of serrations of the order of 100 MPa within the strain range of 0.08, with 19 equidistant serrations. This corresponds well to the pattern of regular serrations shown in Fig. 4, during which formation of the subsequent shear bands in grade 316L stainless steel immersed in liquid helium (4.2 K) is observed. It leads to the conclusion, that the oscillations of the stress components in the shear band, illustrated in Fig. 15 a, b, c, d, represent well the serration process that occurs inside the shear band. Moreover, evolution of the Odqvist parameter in the shear band (Fig. 16) indicates favourable conditions for the phase transformation to occur, which has been clearly demonstrated in Fig. 9, and quantified in Table 3. The numerical model incorporates the feature of the plastic strain induced fcc-bcc phase transformation that affects the hardening during each serration. Evolution of the strain components in the course of subsequent serrations is illustrated in Fig. 17.

## 6. Discussion

In the present paper, the problem of shear bands formation, accompanied by the plastic strain induced fcc-bcc phase transformation in the metastable materials at very low temperatures, has been raised. In order to perform a correlation between the intermittent plastic flow (serrated yielding), occurring in the stainless steels strained in the proximity of absolute zero, the regular stage of the stress-strain curve has been accounted for. It is characterized by regular serrations of a constant stress amplitude (Fig. 4), and the stress oscillations occur between the upper and the lower stress levels. Regular (perfect) stage is interpreted as corresponding to the sequential shear band formation, one by one, along the gauge length of the sample. It lasts until the gauge length is entirely consumed by the successive shear bands. Later on, the irregular stage of the deformation process begins. It is accompanied by strong hardening and irregular serrations, and it is not objective of the present paper. Both stages (the regular and the irregular) form entire deformation pattern, and the regular stage is somewhat similar to the "perfect plasticity", whereas the irregular stage resembles "linear hardening" (Fig. 4). The main objective of the present paper consisted in finding a correlation between regular serrations and formation of the successive shear bands, as well as in measuring the amount of secondary phase produced during each serration. Another objective was related to identification of the velocity of the phase transformation front propagation.

In the course of experiments, new evidence has been found for the fact, that each stress oscillation (serration) during the IPF is accompanied by formation of a separate shear band. Moreover, advanced analysis of the martensite content in the shear band performed by means of the feritscope shows, that the amount of the martensite after the first serration reaches 9%, after the second serration 18%, and in the course of subsequent serrations reaches a saturation level of around 36–38%. This indicates that maximum volume fraction of secondary phase in the course of regular stage does not exceed 40%, which is an important conclusion in view of massive applications of 316L stainless steel in the structures operating at extremely low temperatures.

**Table 3**
vol fraction of all three phases indicated in Fig. 9

| Phase | Volume fraction [%] | | |
|---|---|---|---|
| | a) | b) | c) |
| α′ martensite | 2,2 | 1,3 | 1,1 |
| ε martensite | 4,2 | 3,3 | 2,7 |
| γ austenite | 84,2 | 83,9 | 87,3 |
| other | 9,4 | 11,5 | 8,9 |

It is worth pointing out, that the propagation of the phase transformation front takes place from one extremity of the sample to the other, and the propagation velocity (understood as the rate of increasing martensite bandwidth) is equal to 0.07 mm/s. This is another important conclusion, that indicates how fast the shear bands succeed, and how dynamic is the growth of secondary phase within each shear band.

In order to describe the regular stage of the deformation process, new double surface constitutive model has been developed. The serrations occur during the regular stage between the constant levels of stress (upper and lower values), which indicates that in the multiaxial process the stress point in the stress space will oscillate between the yield and the recovery surfaces, as indicated in Fig. 14. Both surfaces were defined on the basis of the available experiments. The plastic flow within single serration is accompanied by the nonlinear hardening, caused by the plastic strain induced fcc-bcc phase transformation. The yield surface moves in the stress space due to the mixed, kinematic and isotropic hardening, whereas the recovery surface remains unchanged. Also, the yield surface starts within each serration from the same position in the stress space, which has been confirmed by the available experimental data. The mechanism of hardening within each serration contains essentially two components: the interaction of dislocations with the inclusions, and the evolution of stiffness due to the increasing fraction of the secondary phase. Both hardening components affect the tangent stiffness operator of two-phase continuum and make the hardening law highly nonlinear.

The results obtained during the numerical analysis correlate quite well with the experimental data. In particular, the amplitude and the frequency of the stress-strain oscillations correspond well to the values obtained during the experiments. The stress oscillations illustrated in Fig. 16e show the amplitude of serrations of the order of 100 MPa, with

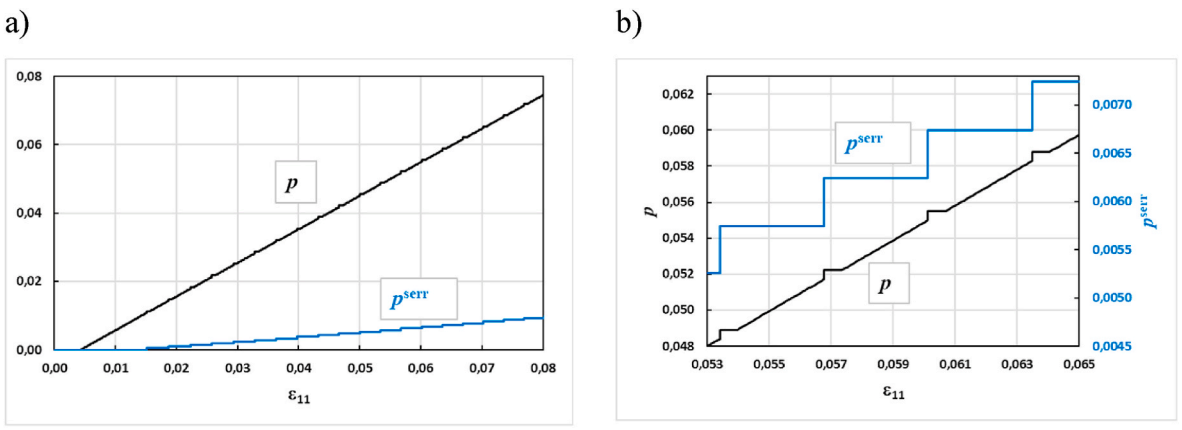


**Fig. 16.** (a) The Odqvist parameter $p$, and (b) the serration Odqvist parameter $p^{serr}$ in the shear band, both invariant with respect to the rotation angle α (defined with respect to tension direction).

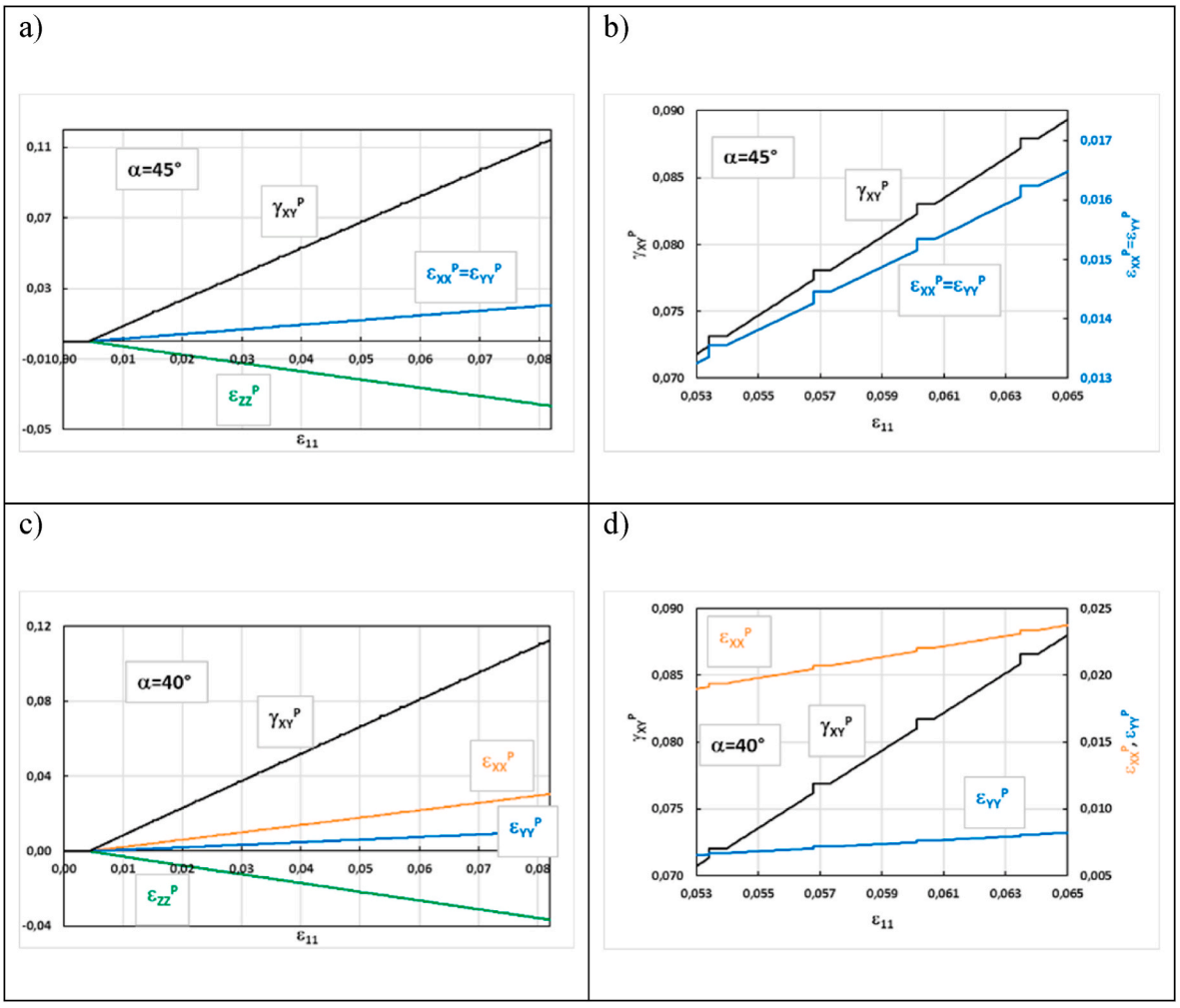


**Fig. 17.** The plastic strains in the shear band rotated by α with respect to tension direction.

19 equidistant serrations over the strain range of 8%. This corresponds quite well to the regular serrations shown in Fig. 4. Numerical convergence with the experimental data indicates that the model is robust, even if the intermittent plastic flow coupled with the plastic strain induced phase transformation remains rather complex from the constitutive and the numerical points of view. One of the interesting achievements is definitely confirmation of the fact, that each serration is associated with formation of an additional shear band. Moreover, propagation of the shear bands along the sample in the course of successive serrations has been clearly demonstrated. Finally, the occurrence of the plastic strain induced fcc-bcc phase transformation during the shear band formation at extremely low temperatures has been demonstrated, which removes doubts expressed in the past in the literature.

## 7. Conclusions

The present paper refers to the process of shear bands formation in the context of the intermittent plastic flow (serrated yielding), coupled with the plastic strain induced fcc-bcc phase transformation, at extremely low temperatures. Formation of the adiabatic shear bands is correlated to the occurrence of the intermittent plastic flow in the stainless steels strained in liquid helium (4.2 K). Novel double surface constitutive model of the intermittent plastic flow includes the classical type Huber-Mises-Hencky yield surface, and a recovery surface (new concept), that reflects the lower bound of the stress oscillations. Mixed kinematic-isotropic, nonlinear hardening, resulting from the evolution of the microstructure of two-phase continuum in the course of the phase transformation, has been applied. The serrations occur between the yield and the recovery surfaces, with the yield surface returning to its initial position at the end of each serration. The model reflects the stress-strain oscillations during the regular stage of the intermittent plastic flow, remaining within the small strains range. Each serration corresponds to formation of an additional shear band there, where the easy slip planes are available. The model has been successfully correlated to the experimental data. Based on the above results, the following conclusions can be drawn:

- The stress-strain curve of grade 316L stainless steel contains two stages: the regular (perfect) and the irregular (hardening).
- The experimental evidence has been found that each serration within the regular stage is accompanied by a shear band formation.
- The smooth plastic flow and the macroscopic slip, contribute to formation of the stacking fault boundles, and result in the plastic strain induced fcc-bcc phase transformation.
- The amount of the secondary phase per single serration has been measured for grade 316L stainless steel, and the overall volume fraction of martensite, after the subsequent serrations within stage 1, does not exceed 40%.
- Apparent propagation of the phase transformation front, corresponding to the occurrence of the subsequent shear bands, was observed. The velocity of the transformation front was measured (0.07 mm/s).
- A novel feature of the constitutive model consists in developing double surface approach in plasticity, comprising the yield and the

recovery surfaces, that represent the bounds for the oscillatory plastic flow in the stress space.

Finally, evidence for the occurrence of the plastic strain induced fcc-bcc phase transformation during the nucleation and the formation of the shear bands at extremely low temperatures, as well as development of the novel double surface constitutive model of the intermittent plastic flow, are new achievements not yet reported in the literature. In the future, development of a distortional model is anticipated, as soon as the experimental work on the shape and the evolution of yield surface is concluded (cf. Distortional plasticity framework including anisotropic hardening, Barlat et al., 2020).

## Declaration of competing interest

The authors declare that they have no known competing financial interests or personal relationships that could have appeared to influence the work reported in this paper.

## Data availability

Data will be made available on request.

## Acknowledgements

The research has been supported by the project of the National Science Centre (NCN), Poland: UMO-2017/27/B/ST8/00298. Also, the research was carried out as part by the project of the National Centre for Research and Development (NCBR), Poland: "ROAD TO EXCELLENCE - a comprehensive university support programme" implemented under the Operational Programme Knowledge Education Development 2014–2020 co-financed by the European Social Fund; agreement no. POWR.03.05.00–00-Z214/18/.

## Annex I.

The following set of parameters was applied during the numerical analysis (Table 4):

**Table 4**
The values of parameters adopted for numerical analysis:

| parameter | | equation | value |
|---|---|---|---|
| $\tau_0$ | internal lattice friction | *Eq.* (14) | $\frac{\sigma_{pl0}}{M}=\frac{9\bullet 10^8}{3}$ [Pa] |
| $\mu$ | shear modulus | *Eq.* (14) | $\frac{E_0}{2(1+\nu)}=\frac{2.1\bullet 10^{11}}{2(1+0.3)}$ [Pa] |
| $\alpha$ | dislocations interaction factor | *Eq.*(14) | 0.4 |
| $b$ | length of the Burgers vector | *Eq.* (9) | $2.58\bullet 10^{-8}$[m] |
| $d$ | average grain size | *Eq.* (10) | $5\bullet 10^{-6}$[m] |
| $k_1$ | constant | *Eq.* (10) | 0.25 |
| $k_2$ | constant | *Eq.*(16) | 0.01 |
| $k_a$ | dislocation annihilation constant | *Eq.* (9) | 0.01 |
| $B_0$ | initial value of density of the lattice barriers | Eqs. 10 and 57 | $5\bullet 10^{12}\left[\frac{1}{m^2}\right]$ |
| $\rho_0$ | initial density of dislocations | Eq. 8 and 57 | $5\bullet 10^{12}\left[\frac{1}{m^2}\right]$ |
| $p_{B0}$ | initial plastic strain intensity threshold for the evolution of the lattice barriers | Eq. 6 and 57 | 0.01 |
| $B_{cr}$ | critical value of density of the lattice barriers | Eq. (17) | $4\bullet 10^{13}\left[\frac{1}{m^2}\right]$ |
| $\tau_{cr}$ | critical value of shear stress at the head of dislocation pile-up | Eq. (17) | $90\bullet\tau_0$ |

The following numerical algorithm has been used in order to carry out the numerical analysis:

I Transformation rule

The transformation rule between the sample principal directions and the rotated shear band directions reads (for stresses):

$$\sigma_{11}=\sigma_{xx}\cos^2\alpha+\sigma_{yy}\sin^2\alpha-\sigma_{xy}\sin 2\alpha \tag{55}$$

$$\sigma_{22}=\sigma_{xx}\sin^2\alpha+\sigma_{yy}\cos^2\alpha+\sigma_{xy}\sin 2\alpha\sigma_{12}=0.5\bullet\sin 2\alpha\left(\sigma_{xx}-\sigma_{yy}\right)+\sigma_{xy}\left(\cos^2\alpha-\sin^2\alpha\right)\sigma_{33}=\sigma_{zz}$$

and for strains:

$$\varepsilon_{11}=\varepsilon_{xx}\cos^2\alpha+\varepsilon_{yy}\sin^2\alpha-0.5\bullet\gamma_{xy}\sin 2\alpha \tag{56}$$

$$\varepsilon_{22}=\varepsilon_{xx}\sin^2\alpha+\varepsilon_{yy}\cos^2\alpha+0.5\bullet\gamma_{xy}\sin 2\alpha\varepsilon_{12}=0.5\bullet\sin 2\alpha\left(\varepsilon_{xx}-\varepsilon_{yy}\right)+0.5\bullet\gamma_{xy}\left(\cos^2\alpha-\sin^2\alpha\right)\varepsilon_{33}=\varepsilon_{zz}$$

In what follows $E$ denotes the elasticity modulus, $\mu$ stands for the shear modulus, $\nu$ is the Poisson ratio and $\sigma_p(p)$ is used for the function of increasing yield limit (hardening).

II Initial state

At the beginning of the integration algorithm, the initial „zero" state is assumed. The stresses and the strains (the total and the plastic parts) are equal to zero. So are the total Odqvist parameter and the serration Odqvist parameter. The microstructure parameters are set to the initial values: the

density of dislocations, the density of the lattice barriers (locks), the fraction of the secondary phase (martensite) and the limit value of the Odqvist parameter for the evolution of the locks to start.

$$\varepsilon_{11} = 0 \tag{57}$$

$$\sigma_{xx} = \sigma_{yy} = \sigma_{xy} = \sigma_{zz} = 0\ \varepsilon_{xx} = \varepsilon_{yy} = \gamma_{xy} = \varepsilon_{zz} = 0\ \varepsilon^{p}_{xx} = \varepsilon^{p}_{yy} = \gamma^{p}_{xy} = \varepsilon^{p}_{zz} = 0$$

$$p = p^{serr} = 0$$

$$\rho = \rho_0, B_0 = B_{00}, B = B_0, \xi = \xi_0, p_B = p^0_B$$

The process is assumed strain-controlled. The maximum value of the principal strain is established, the number of the load steps is assumed and the constant value of the total strain increment is calculated.

$$\Delta\varepsilon_{11} = \frac{\varepsilon^{max}_{11}}{\underset{step}{l}} = const \tag{58}$$

In general, three stages of the deformation process are cyclically repeated: (1) elastic (either initial or after-serration), followed by (2) continues plastic flow ended by (3) serration, followed again by the elastic range.

III Elastic deformation

Strain increments:

$$\Delta\varepsilon_{22} = \Delta\varepsilon_{33} = -\nu \bullet \Delta\varepsilon_{11} \tag{59}$$

strain increments in the band:

$$\Delta\varepsilon_{xx} = \Delta\varepsilon_{11} \bullet \left(\cos^2\alpha - \nu\sin^2\alpha\right) \tag{60}$$

$$\Delta\varepsilon_{yy} = \Delta\varepsilon_{11} \bullet \left(\sin^2\alpha - \nu\cos^2\alpha\right)$$

$$\Delta\gamma_{xy} = -\Delta\varepsilon_{11} \bullet (1+\nu) sin\ 2\alpha \Delta\varepsilon_{zz} = \Delta\varepsilon_{33}$$

stress increments in the shear band (linear elasticity law):

$$\Delta\sigma_{xx} = \frac{2\mu(1-\nu)}{1-2\nu}\Delta\varepsilon_{xx} + \frac{2\mu\nu}{1-2\nu}\left(\Delta\varepsilon_{yy} + \Delta\varepsilon_{zz}\right) \tag{61}$$

$$\Delta\sigma_{yy} = \frac{2\mu(1-\nu)}{1-2\nu}\Delta\varepsilon_{yy} + \frac{2\mu\nu}{1-2\nu}(\Delta\varepsilon_{xx} + \Delta\varepsilon_{zz})\Delta\sigma_{xy} = \mu\Delta\gamma_{xy}\Delta\sigma_{zz} = \frac{2\mu(1-\nu)}{1-2\nu}\Delta\varepsilon_{zz} + \frac{2\mu\nu}{1-2\nu}\left(\Delta\varepsilon_{xx} + \Delta\varepsilon_{yy}\right) \equiv 0$$

check elastic limit:

If

$$\Phi = (\sigma_{xx} + \Delta\sigma_{xx})^2 + \left(\sigma_{yy} + \Delta\sigma_{yy}\right)^2 - (\sigma_{xx} + \Delta\sigma_{xx})\left(\sigma_{yy} + \Delta\sigma_{yy}\right) + 3\left(\sigma_{xy} + \Delta\sigma_{xy}\right)^2 - \left(\sigma_p(p)\right)^2 > 0 \tag{62}$$

then.

Reduce

$$\Delta\varepsilon_{11} \leftarrow \beta\Delta\varepsilon_{11}, 0 < \beta < 1 \tag{63}$$

$$a_o = \sigma^2_{xx} - \sigma_{xx}\sigma_{yy} + \sigma^2_{yy} + 3\sigma^2_{xy} - \left(\sigma_p(p)\right)^2 \tag{64}$$

$$a_1 = 2\sigma_{xx} \bullet \Delta\sigma_{xx} - \sigma_{xx} \bullet \Delta\sigma_{yy} - \sigma_{yy} \bullet \Delta\sigma_{xx} + 2\sigma_{yy} \bullet \Delta\sigma_{yy} + 6\sigma_{xy} \bullet \Delta\sigma_{xy}\ a_2 = (\Delta\sigma_{xx})^2 - \Delta\sigma_{xx} \bullet \Delta\sigma_{yy} + \left(\Delta\sigma_{yy}\right)^2 + 3\left(\Delta\sigma_{xy}\right)^2\ \beta = \frac{-a_1 + \sqrt{a_1^2 - 4a_2 \bullet a_0}}{2a_2}$$

go back to (59) so as to obtain $\Phi = 0$ (exact end of the elastic range), and update the strains and the stresses:

$$\varepsilon_{xx} \leftarrow \varepsilon_{xx} + \Delta\varepsilon_{xx};\ \varepsilon_{yy} \leftarrow \varepsilon_{yy} + \Delta\varepsilon_{yy};\ \gamma_{xy} \leftarrow \gamma_{xy} + \Delta\gamma_{xy};\ \varepsilon_{zz} \leftarrow \varepsilon_{zz} + \Delta\varepsilon_{zz} \tag{65}$$

$$\sigma_{xx} \leftarrow \sigma_{xx} + \Delta\sigma_{xx};\ \sigma_{yy} \leftarrow \sigma_{yy} + \Delta\sigma_{yy};\ \sigma_{xy} \leftarrow \sigma_{xy} + \Delta\tau_{xy};\ \sigma_{zz} \leftarrow \sigma_{zz}$$

back transformation to the principal direction:

$$\varepsilon_{11} = \varepsilon_{xx}\cos^2\alpha + \varepsilon_{yy}\sin^2\alpha - 0.5 \bullet \gamma_{xy}\sin 2\alpha \tag{66}$$

If $\varepsilon_{11} \geq \varepsilon^{max}_{11}$ then **stop**If $\Phi < 0$ then continue from (62) else $\Delta\varepsilon_{11} = \frac{\varepsilon^{max}_{11}}{\underset{step}{l}}$ and continue from (67).

IV Plastic deformation

Assume (iteration starts):

$$\Delta\varepsilon_{22} = \Delta\varepsilon_{33} = -\nu \bullet \Delta\varepsilon_{11} \tag{67}$$

strain increments in the band:

$$\Delta\varepsilon_{xx} = \Delta\varepsilon_{11} \bullet \cos^2\alpha + \Delta\varepsilon_{22} \bullet \sin^2\alpha \tag{68}$$

$$\Delta\varepsilon_{yy} = \Delta\varepsilon_{11} \bullet \sin^2\alpha + \Delta\varepsilon_{22} \bullet \cos^2\alpha$$

$$\Delta\gamma_{xy} = -(\Delta\varepsilon_{11} - \Delta\varepsilon_{22})\sin 2\alpha$$

$$\Delta\varepsilon_{zz} = \Delta\varepsilon_{33}$$

elastic predictor for stresses:

$$\sigma^*_{xx} = \sigma_{xx} + \frac{2\mu(1-\nu)}{1-2\nu}\Delta\varepsilon_{xx} + \frac{2\mu\nu}{1-2\nu}\left(\Delta\varepsilon_{yy} + \Delta\varepsilon_{zz}\right) \tag{69}$$

$$\sigma^*_{yy} = \sigma_{yy} + \frac{2\mu(1-\nu)}{1-2\nu}\Delta\varepsilon_{yy} + \frac{2\mu\nu}{1-2\nu}\left(\Delta\varepsilon_{xx} + \Delta\varepsilon_{zz}\right)\ \sigma^*_{xy} = \sigma_{xy} + \mu\Delta\gamma_{xy}\ \sigma^*_{zz} = \sigma_{zz} + \frac{2\mu(1-\nu)}{1-2\nu}\Delta\varepsilon_{zz} + \frac{2\mu\nu}{1-2\nu}\left(\Delta\varepsilon_{xx} + \Delta\varepsilon_{yy}\right)$$

assume plastic multiplier $\Delta\lambda = 0$ (iteration starts):

$$s1_{xy} = \sigma^*_{xx} + \sigma^*_{yy} - \Delta\lambda\frac{2\mu}{1+\Delta\lambda 6\mu}\left(\sigma^*_{xx} + \sigma^*_{yy} - 2\sigma^*_{zz}\right) \tag{70}$$

$$s1_{xz} = \sigma^*_{xx} + \sigma^*_{zz} - \Delta\lambda\frac{2\mu}{1+\Delta\lambda 6\mu}\left(\sigma^*_{xx} + \sigma^*_{zz} - 2\sigma^*_{yy}\right)$$

$$s2_{xy} = \frac{\sigma^*_{xx} - \sigma^*_{yy}}{1+\Delta\lambda 6\mu}, s2_{xz} = \frac{\sigma^*_{xx} - \sigma^*_{zz}}{1+\Delta\lambda 6\mu}$$

plastic relaxation:

$$\sigma_{xx} \leftarrow \frac{s1_{xy} + s2_{xy}}{2}, \sigma_{yy} \leftarrow \frac{s1_{xy} - s2_{xy}}{2}, \sigma_{zz} \leftarrow \frac{s1_{xz} - s2_{xz}}{2}, \sigma_{xy} \leftarrow \frac{\sigma^*_{xy}}{1+\Delta\lambda 6\mu} \tag{71}$$

$$\Delta\varepsilon^{\mathrm{p}}_{ij} = \Delta\lambda\frac{\partial\Phi}{\partial\sigma_{ij}}$$

$$\Delta\varepsilon^{\mathrm{p}}_{xx} \leftarrow \Delta\lambda \bullet \left(2\sigma_{xx} - \sigma_{yy} - \sigma_{zz}\right)\Delta\varepsilon^{\mathrm{p}}_{yy} \leftarrow \Delta\lambda \bullet \left(2\sigma_{yy} - \sigma_{zz} - \sigma_{xx}\right)\Delta\varepsilon^{\mathrm{p}}_{zz} \leftarrow \Delta\lambda \bullet \left(2\sigma_{zz} - \sigma_{xx} - \sigma_{yy}\right) \equiv \Delta\varepsilon^{\mathrm{p}}_{zz} \leftarrow -\Delta\varepsilon^{\mathrm{p}}_{xx} - \Delta\varepsilon^{\mathrm{p}}_{yy}\Delta\gamma^{\mathrm{p}}_{xy} \leftarrow \Delta\lambda$$

$$\bullet\ 6\sigma_{xy}\ \varepsilon_{zz} \leftarrow \frac{\sigma_{zz}}{E} - \frac{\nu}{E}\left(\sigma_{xx} + \sigma_{yy}\right) + \varepsilon^{\mathrm{p}}_{zz} + \Delta\varepsilon^{\mathrm{p}}_{zz}\Delta p = \sqrt{\frac{2}{3}\left(\Delta\varepsilon^{\mathrm{p}\,2}_{xx} + \Delta\varepsilon^{\mathrm{p}\,2}_{yy} + \Delta\varepsilon^{\mathrm{p}\,2}_{zz} + 0.5\Delta\gamma^{\mathrm{p}\,2}_{xy}\right)}$$

If $\Phi = \sqrt{\sigma^2_{xx} + \sigma^2_{yy} + \sigma^2_{zz} - \sigma_{xx}\sigma_{yy} - \sigma_{yy}\sigma_{zz} - \sigma_{zz}\sigma_{xx} + 3\sigma^2_{xy}} - \sigma_{\mathrm{p}}(p + \Delta p) \neq 0$

Then

Change $\Delta\lambda$ (the Newton method) and loop back to (70) until $\Phi = 0$ (return mapping)

Back transformation to (1, 2, 3):

$$\sigma_{22} \leftarrow \sigma_{xx} \bullet \sin^2\alpha + \sigma_{yy} \bullet \cos^2\alpha + \sigma_{xy} \bullet \sin 2\alpha, \sigma_{33} \leftarrow \sigma_{zz} \tag{72}$$

If $\sigma_{22} \neq 0$ or $\sigma_{33} \neq 0$

Then

Change $\Delta\varepsilon_{22}$ and $\Delta\varepsilon_{33}$ (the Newton method), and loop back to (68) until $\sigma_{22} = 0$ and $\sigma_{33} = 0$

Update total strains and plastic strains:

$$\varepsilon_{xx} \leftarrow \varepsilon_{xx} + \Delta\varepsilon_{xx};\ \varepsilon_{yy} \leftarrow \varepsilon_{yy} + \Delta\varepsilon_{yy};\ \gamma_{xy} \leftarrow \gamma_{xy} + \Delta\gamma_{xy}; \tag{73}$$

$$\varepsilon^{\mathrm{p}}_{xx} \leftarrow \varepsilon^{\mathrm{p}}_{xx} + \Delta\varepsilon^{\mathrm{p}}_{xx};\ \varepsilon^{\mathrm{p}}_{yy} \leftarrow \varepsilon^{\mathrm{p}}_{yy} + \Delta\varepsilon^{\mathrm{p}}_{yy};\ \varepsilon^{\mathrm{p}}_{zz} \leftarrow \varepsilon^{\mathrm{p}}_{zz} + \Delta\varepsilon^{\mathrm{p}}_{zz};\ \gamma^{\mathrm{p}}_{xy} \leftarrow \gamma^{\mathrm{p}}_{xy} + \Delta\gamma^{\mathrm{p}}_{xy};$$

update the Odqvist parameter and the actual equivalent stress (yield stress):

$$p \leftarrow p + \Delta p, \sigma_{\mathrm{eqv}} = \sqrt{\sigma^2_{xx} + \sigma^2_{yy} - \sigma_{xx}\sigma_{yy} + 3\sigma^2_{xy}} \tag{74}$$

update the lattice barriers (locks) density:

$$\text{if } p > p_{\mathrm{B}} \text{ then } B \leftarrow \min\left(B + F_{\mathrm{B}}^{+}\left(\rho, \sigma_{\mathrm{eqv}}\right) \bullet \Delta p; B_{\mathrm{cr}}\right) \tag{75}$$

Update the phase volume fraction:

$$\text{if } \left(p > \varepsilon_{\xi}^{p}\right) \wedge \left(p < \varepsilon_{L}^{p}\right) \text{ then } \xi \leftarrow \xi + A \bullet \Delta p \tag{76}$$

Update the density of dislocations, the average shear stress in the lattice, the mean free path of dislocations and the shear stress at the head of dislocation pile-up:

$$\rho \leftarrow \rho + M\left(\frac{1}{db} + \frac{k_1\sqrt{\rho}}{b} - k_{\mathrm{a}}\rho\right)\Delta p \tag{77}$$

$$\tau_{\mathrm{av}} = \tau_0 + \mu\alpha b\sqrt{\rho}\ (\overline{\Lambda})^{-1} = d^{-1} + k_1\sqrt{\rho} + k_2\sqrt{B}\ \tau_{\mathrm{e}} = \pi(1-\nu)(\mu b)^{-1}\overline{\Lambda}\tau_{\mathrm{av}}^2$$

check the serration condition:

If

$$\left\{\begin{array}{c} [\tau_{\mathrm{e}} \le \tau_{\min} \wedge B = B_{\mathrm{cr}}] \vee \\ [B \le B_{\min} \wedge \tau_{\mathrm{e}} = \tau_{\mathrm{cr}}] \vee \\ [\tau_{\mathrm{e}} > \tau_{\min} \wedge B > B_{\min} \wedge (B - B_{\min})(\tau_{\min} - \tau_{\mathrm{cr}}) - (B_{\mathrm{cr}} - B_{\min})(\tau_{\mathrm{e}} - \tau_{\mathrm{cr}}) = 0] \end{array}\right\}$$

Then serration (continue from Eq. (79)).

Else back transformation to the principal direction:

$$\varepsilon_{11} = \varepsilon_{xx}\cos^2\alpha + \varepsilon_{yy}\sin^2\alpha - 0.5 \bullet \gamma_{xy}\sin 2\alpha \tag{78}$$

$$\text{if } \varepsilon_{11} \ge \varepsilon_{11}^{\max} \text{ then } \textbf{stop} \text{ else continue from } (67).$$

V Serration

Reduce stresses down to recovery surface:

$$\kappa = \frac{\sigma_{\mathrm{r}}}{\sigma_{\mathrm{eqv}}} - 1 \tag{79}$$

$$\Delta\sigma_{xx}^{\mathrm{r}} = \kappa \bullet \sigma_{xx};\ \Delta\sigma_{yy}^{\mathrm{r}} = \kappa \bullet \sigma_{yy};\ \Delta\sigma_{xy}^{\mathrm{r}} = \kappa \bullet \sigma_{xy};\ \Delta\sigma_{zz}^{\mathrm{r}} = 0$$

calculate the plastic strain increments, as well as the Odqvist parameter increment due to serration:

$$\Delta\varepsilon_{xx}^{\mathrm{p,serr}} = -\frac{\Delta\sigma_{xx}^{\mathrm{r}} - \nu \bullet \Delta\sigma_{yy}^{\mathrm{r}}}{E} \tag{80}$$

$$\Delta\varepsilon_{yy}^{\mathrm{p,serr}} = -\frac{\Delta\sigma_{yy}^{\mathrm{r}} - \nu \bullet \Delta\sigma_{xx}^{\mathrm{r}}}{E}\Delta\varepsilon_{zz}^{\mathrm{p,serr}} = \frac{\nu \bullet \left(\Delta\sigma_{xx}^{\mathrm{r}} + \Delta\sigma_{yy}^{\mathrm{r}}\right)}{E}\Delta\gamma_{xy}^{\mathrm{p,serr}} = -\frac{\Delta\sigma_{xy}^{\mathrm{r}}}{G}\Delta p^{\mathrm{serr}} = \sqrt{\frac{2}{3}\left(\Delta\varepsilon_{xx}^{\mathrm{p,serr}\,2} + \Delta\varepsilon_{yy}^{\mathrm{p,serr}\,2} + \Delta\varepsilon_{zz}^{\mathrm{p,serr}\,2} + 0.5\Delta\gamma_{xy}^{\mathrm{p,serr}\,2}\right)}$$

keep the total strains unchanged, update the in-plane stresses, update the plastic strains:

$$\sigma_{xx} \leftarrow \sigma_{xx} + \Delta\sigma_{xx}^{\mathrm{r}};\ \ \sigma_{yy} \leftarrow \sigma_{yy} + \Delta\sigma_{yy}^{\mathrm{r}};\ \ \sigma_{xy} \leftarrow \sigma_{xy} + \Delta\sigma_{xy}^{\mathrm{r}} \tag{81}$$

$$\varepsilon_{xx}^{\mathrm{p}} \leftarrow \varepsilon_{xx}^{\mathrm{p}} + \Delta\varepsilon_{xx}^{\mathrm{p,serr}};\ \ \varepsilon_{yy}^{\mathrm{p}} \leftarrow \varepsilon_{yy}^{\mathrm{p}} + \Delta\varepsilon_{yy}^{\mathrm{p,serr}};\ \ \varepsilon_{zz}^{\mathrm{p}} \leftarrow \varepsilon_{zz}^{\mathrm{p}} + \Delta\varepsilon_{zz}^{\mathrm{p,serr}};\ \ \ \gamma_{xy}^{\mathrm{p}} = \gamma_{xy}^{\mathrm{p}} + \Delta\gamma_{xy}^{\mathrm{p,serr}}$$

update the Odqvist parameter and the serration Odqvist parameter:

$$p \leftarrow p + \Delta p^{\mathrm{serr}};\ \ \ p^{\mathrm{serr}} \leftarrow p^{\mathrm{serr}} + \Delta p^{\mathrm{serr}} \tag{82}$$

update the phase volume fraction:

$$\text{if } \left(p > \varepsilon_{\xi}^{p}\right) \wedge \left(p < \varepsilon_{L}^{p}\right) \text{ then } \xi \leftarrow \xi + A \bullet \Delta p^{\mathrm{serr}} \tag{83}$$

Update the after-serration parameters (the density of lattice barriers (locks), the density of dislocations, the limit value of the Odqvist parameter for the barriers to start to evolve):

$$B_0 \leftarrow 1.02 \bullet B_0;\ \ \ B = B_0;\ \ \ \rho \leftarrow \rho_0 \tag{84}$$

$$p_{\mathrm{B}} \leftarrow p + p_{\mathrm{B}}^0;\ \ \ p_{\mathrm{B}}^0 \leftarrow p_{\mathrm{B}}^0 \bullet 0.95$$

continue from (59).

## References


Basinski, Z.S., 1957. The instability of plastic flow of metals at very low temperatures. Proc. Roy. Soc. London Series A 240, 229–242.

Barlat, F., Yoon, S., Lee, S., Wi, M., Kim, J., 2020. Distortional plasticity framework with application to advanced high strength steel. Int. J. Solid Struct. 202, 947–962.

Bayerlein, M., Mughrabi, H., Kesten, M., Meier, B., 1992. Improvement of the strength of a metastable austenitic stainless steel by cyclic deformation-induced martensitic transformation at 103 K. Mater. Sci. Eng. 159, 35–41.

Böhm, H., 1998. A Short Introduction to Basic Aspects of Continuum Micromechanics. TU Wien, Vienna.

Bracke, L., Kestens, L., Penning, J., 2007. Transformation mechanism of α′-martensite in an austenitic Fe–Mn–C–N alloy. Scripta Mater. 57, 385–388.

Brechtl, J., Chen, S.Y., Xieb, X., Renc, Y., Qiaod, J.W., Liaw, P.K., Zinkle, S.J., 2019. Towards a greater understanding of serrated flows in an Al containing high-entropy-based alloy. Int. J. Plast. 115, 71–92.

Burns, T.J., 1994. A simple criterion for the onset of discontinuous plastic deformation in metals at very low temperatures. J. Mech. Phys. Solid. 42, 797–811.

Chaboche, J., Kanouté, P., 2003. Sur les approximations « isotrope » et « anisotrope » de l'opérateur tangent pour les méthodes tangentes incrémentale et affine. Compt. Rendus Mec. 331, 857–864.

Cherkaoui, M., Berveiller, M., Sabar, H., 1998. Micromechanical modeling of martensitic transformation induced plasticity (TRIP) in austenitic single crystals. Int. J. Plast. 14, 597–626.

Das, A., Tarafder, S., 2009. Experimental investigation on martensitic transformation and fracture morphologies of austenitic stainless steel. Int. J. Plast. 25, 2222–2247.

Diani, J.M., Parks, D.M., 1998. Effects of strain state on the kinetics of strain-induced martensite in steels. J. Mech. Phys. Solid. 46, 1613–1635.

Doghri, I., Ouaar, A., 2003. Homogenization of two-phase elasto-plastic composite materials and structures: study of tangent operators, cyclic plasticity and numerical algorithms. Int. J. Solid Struct. 40, 1681–1712.

Estrin, Y., Kubin, L.P., 1980. Criterion for thermomechanical instability of low temperature plastic deformation. Scripta Metall. 14, 1359–1364.

Estrin, Y., Tangri, K., 1981. Thermal mechanism of the anomalous temperature dependence of the flow stress. Scripta Metall. 15, 1323–1328.

Garion, C., Skoczeń, B., Sgobba, S., 2006. Constitutive modelling and identification of parameters of the plastic strain-induced martensitic transformation in 316L stainless steel at cryogenic temperatures. Int. J. Plast. 22, 1234–1264.

Gröger, V., Zehetbauer, M., 1993. Onset mechanisms of discontinuous flow at low temperatures in one- and two-phase Cu·Be alloys. Mater. Sci. Eng. 164 (1–2), 240–245.

Han, W., Liu, Y., Wan, F., Liu, P., Yi, X., Zhan, Q., Morrall, D., Ohnuki, S., 2018. Deformation behavior of austenitic stainless steel at deep cryogenic temperatures. J. Nucl. Mater. 504, 29–32.

Kim, J.-H., Kim, S.-K., Lee, C.-S., Kim, M.-H., Lee, J.-M., 2014. A constitutive equation for predicting the material nonlinear behavior of AISI 316L, 321, and 347 stainless steel under low-temperature conditions. Int. J. Mech. Sci. 87, 218–225.

Kocks, U.F., Mecking, H., 2003. The physics and phenomenology of strain hardening. Prog. Mater. Sci. 48 (3), 171–273.

Komnik, S.N., Demirsky, V.V., Startsev, V.I., 1985. Low temperature instability of plastic flow of alloys. Czech. J. Phys. B 35, 230–234.

Kubin, L.P., Spiesser, Ph, Estrin, Y., 1982. Computer simulation of the low temperature instability of plastic flow. Acta Metall. 30 (2), 385–394.

Ma, A., Roters, F., Raabe, D., 2006. A dislocation density based constitutive model for crystal plasticity FEM including geometrically necessary dislocations. Acta Mater. 54, 2169–2179.

Mróz, Z., 1967. On the description of anisotropic workhardening. J. Mech. Phys. Solid. 15, 163–175.

Obst, B., Nyilas, A., 1991. Experimental evidence on the dislocation mechanism of serrated yielding in f.c.c. metals and alloys at low temperatures. Mater. Sci. Eng. 137, 141–150.

Obst, B., Nyilas, A., 1998. Time-resolved flow stress behavior of structural materials at low temperatures. In: Advances in Cryogenic Engineering, vol. 44. Plenum Press, New York, pp. 331–338.

Olson, G.B., Cohen, M., 1972. A mechanism for the strain-induced nucleation of martensitic transformations. J. Less Common Met. 28, 107–118.

Olson, G.B., Cohen, M., 1975. Kinetics of strain-induced martensitic nucleation. Metall. Trans. A 6, 791.

Ortolano González, J.M., Hernández Ortega, J.A., Oliver Olivella, X., 2013. A comparative study on homogenization strategies for multi-scale analysis of materials. Centre Internacional de Mètodes Numèrics en Enginyeria (CIMNE).

Ortwein, R., Skoczeń, B., Tock, J.P., 2014. Micromechanics based constitutive modeling of martensitic transformation in metastable materials subjected to torsion at cryogenic temperatures. Int. J. Plast. 59, 152–179.

Ottosen, N.S., Ristinmaa, M., 2005. The mechanics of Constitutive modeling. Elsevier Science.

Pierard, O., Doghri, I., 2006. Study of various estimates of the macroscopic tangent operator in the incremental homogenization of elastoplastic composites. Int. J. Multiscale Comput. Eng. 4, 521–543.

Préve, D., Bacigalupo, A., Paggi, M., 2021. Variational-asymptotic homogenization of thermoelastic periodic materials with thermal relaxation. Int. J. Mech. Sci. in press.

Pustovalov, V.V., 2008. Serrated deformation of metals and alloys at low temperatures. Low Temp. Phys. 34, 683–723.

Seeger, A., 1957. Dislocations and mechanical properties of crystals. Wiley, New York.

Shibata, K., 1988. Discussion about Basinski's model for serration at very low temperatures. Cryogen. Mater. 88, 865–872.

Sitko, M., Skoczeń, B., Wróblewski, A., 2010. FCC–BCC phase transformation in rectangular beams subjected to plastic straining at cryogenic temperatures. Int. J. Mech. Sci. 52, 993–1007.

Skoczeń, B., Bielski, J., Sgobba, S., Marcinek, D., 2010. Constitutive model of discontinuous plastic flow at cryogenic temperatures. Int. J. Plast. 26, 1659–1679.

Skoczeń, B., Bielski, J., Tabin, J., 2014. Multiaxial constitutive model of discontinuous plastic flow at cryogenic temperatures. Int. J. Plast. 55, 198–218.

Tabin, J., Skoczen, B., Bielski, J., 2016. Strain localization during discontinuous plastic flow at extremely low temperatures. Int. J. Solid Struct. 97–98, 593–612.

Tabin, J., Skoczen, B., Bielski, J., 2021. Discontinuous plastic flow in stainless steels subjected to combined loads at extremely low temperatures. Int. J. Mech. Sci. 200, 14.

Tandon, G.P., Weng, G.J., 1988. A theory of particle-reinforced plasticity. J. Appl. Mech. 55, 126–135.

Tirunilai, A.S., Hanemann, T., Weiss, K.P., Freudenberger, J., Heilmaier, M., Kauffmann, A., 2020. Dislocation-based serrated plastic flow of high entropy alloys at cryogenic temperatures. Acta Mater. 200, 980–991.

Vinogradov, A., Lazarev, A., Louzguine-Luzgin, D.V., Yokoyama, Y., Yavarid, A.R., Inoue, A., 2010. Propagation of shear bands in metallic glasses and transition from serrated to non-serrated plastic flow at low temperatures. Acta Mater. 58 (20), 6736–6743.

Vorob'ev, E.V., 2006. New types of limit states of structural alloys related to the realization of the low temperature discontinuous yielding effect. Mechanics 57, 17–21.

Vorob'ev, E.V., 2008. Peculiarities of neck formation under low-temperature discontinuous yield of metals. Part 2. Plane strain. Strength Mater. 40, 439–444.

Vorob'ev, E.V., Anpilogova, T.V., 2013. Numerical analysis of the deformation instability of metals in liquid helium. Comput. Mater. Sci. 68, 66–72.

Vorob'ev, E.V., Anpilogova, T.V., 2015. Kinetics of low-temperature discontinuous deformation of metals. Cryogenics 68, 59–66.

Wang, Y.T., Dong, J., Liu, Y.H., Bai, H.Y., Wang, W.H., Sun, B.A., 2020. Optimum shear stability at intermittent-to-smooth transition of plastic flow in metallic glasses at cryogenic temperatures. Materialia 9, 4.

Zaiser, M., Hähner, P., 1997. Oscillatory modes of plastic deformation: theoretical concepts. Phys. Status Solidi 199, 267–330.

Zinov'ev, M.V., Il'ichev, V.Y., Rykov, V.A., Savva, S.P., 1972. Method of testing samples in a biaxial stressed state at low temperatures. Strength Mater. 4, 637–639.